A&A, 714, A210 (2026)
https://doi.org/10.1051/0004-6361/202660141
© The Authors 2026

Astronomy & Astrophysics

Euclid Quick Data Release (Q1)

XLII. Searching for radio-selected *Euclid*-dark galaxies in the EDF-N

Euclid Collaboration: M. Giulietti, I. Prandoni, L. Bisigello, G. Rodighiero, M. Talia, F. Gentile, G. Girardi, M. Bondi, et al.

(Full author list and affiliations details can be found after the references)

Received 30 March 2026 / Accepted 24 June 2026

ABSTRACT

We present and investigate the properties of a sample of radio-selected, *Euclid*-dark galaxies, identified from LOFAR HBA observations at 144 MHz within the Euclid Deep Field-North (EDF-N), covering approximately 10 deg^2. Starting from 1051 radio sources lacking optical counterparts down to a 5σ depth of 23.9 in the y band in previous surveys (but detected with *Spitzer*/IRAC), we identified 166 galaxies with no emission at a depth of more than 3σ from *Euclid* Quick Release 1 (Q1) images, reaching a 5σ depth of 23.9 in the H_E band, and no matches in the *Euclid* Q1 catalogue. To minimise contamination from nearby sources, we selected a sub-sample of 88 isolated galaxies. By exploiting multi-band images and catalogues available for the EDF-N, we inferred the physical properties of our sample via SED fitting. The resulting redshift distribution spans $0.4 \leq z_{ph} \leq 5.0$. We made use of recent sub-arcsecond imaging from the International LOFAR Telescope over an area of 2.5 deg × 2.5 deg to constrain the nature of the compact radio emission in our targets through brightness-temperature estimates. By combining this information with the radio excess relative to the infrared/radio-correlation (IRRC), we searched for possible active galactic nucleus (AGN) activity in our sample. Approximately 30% of our sources show a radio excess relative to star formation. This fraction increases to 40% when including AGNs identified via their brightness temperature. The *Euclid*-dark sources detected in the far-infrared (FIR) are consistent with a population of heavily obscured ($\langle A_V^{ISM} \rangle = 5.0$) massive ($\langle \log_{10}(M_\star/M_\odot) \rangle = 11.6$) star forming galaxies (SFGs) with high star formation rates ($\langle \log_{10}(SFR/M_\odot\,yr^{-1}) \rangle = 3.3$). Their location above the star-forming main sequence is consistent with the high-mass and high-SFR end of similar near-infrared (NIR)-dark galaxy populations selected at higher radio frequencies reported in the literature. We performed a UV-to-radio median stacking analysis, dividing the sources with LOFAR ILT imaging according to the presence of radio excess. Both sub-samples are detected in the H_E band at 3σ and 9σ for the radio-excess and non–radio-excess sources, respectively. The two stacked populations exhibit similar global physical properties and differ primarily in their radio emission, with values consistent with those observed for individual sources, albeit with less extreme SFRs. These preliminary results indicate that, compared to similar selections carried out over smaller fields, the wide area covered by *Euclid* enables the identification of a higher fraction of systems in which intense star formation and AGN activity coexist, likely capturing a key phase of galaxy–black hole co-evolution.

Key words. galaxies: active – galaxies: high-redshift – galaxies: nuclei – galaxies: starburst – galaxies: star formation

1. Introduction

Continuum radio emission is an effective tracer of star formation activity inside galaxies, originating from a combination of the synchrotron emission from electrons accelerated in supernova remnants and free–free continuum radiation from ionised H II regions (e.g. Condon et al. 2002; Kennicutt & Evans 2012). Unlike other star formation tracers, such as the ultraviolet (UV) and H α luminosity, the radio emission is unaffected by dust extinction and can be efficiently exploited to study the dust-obscured star formation (e.g. Chapman et al. 2004). Moreover, in contrast to far-infrared (FIR) observations, which often suffer from source-blending issues, radio surveys can achieve sub-arcsecond angular resolution, considerably improving the reliability of counterpart identification.

Radio selection has proven to be extremely effective in identifying populations of dusty star forming galaxies (SFGs), often missed by optical and near-infrared (NIR) surveys (Chapman et al. 2001; Smail et al. 2002; Talia et al. 2021; Enia et al. 2022; Behiri et al. 2023; van der Vlugt et al. 2023; and Gentile et al. 2024, 2025, defined as G24 and G25 hereafter). Because of their faintness at shorter wavelengths, these extreme objects, and more generally all sources with very weak optical/near-infrared (NIR) emission, are commonly named 'optically dark' galaxies (Simpson et al. 2014; Wang et al. 2019; Gruppioni et al. 2020; Sun et al. 2021; Fudamoto et al. 2021; Smail et al. 2021; Shu et al. 2022), but are also referred to as *Hubble* Space Telescope (HST)-dark, radio-selected (Rs)-NIR dark, *H*-dropout, NIR-dark/faint, or optical/NIR (OIR)-dark, depending on their selection criteria (Wang et al. 2016; Franco et al. 2018; Williams et al. 2019a; Gruppioni et al. 2020; Riechers et al. 2020; Manning et al. 2022). Such studies have associated these populations with massive ($M_\star > 10^{10}\,M_\odot$), dust-rich ($A_V > 3$), and high-redshift ($z > 2$–3) galaxies, highlighting their potential impact on the cosmic star formation rate density (SFRD). In particular, their contribution has been estimated to account for up to 40% of the high-redshift SFRD density traced by Lyman-break galaxies (e.g. Talia et al. 2021; Barrufet et al. 2023; Xiao et al. 2023; Xiao et al. 2024; G25).

One major caveat to consider when using the radio band as a tracer of star formation is the potential contamination from active galactic nuclei (AGNs). Indeed, in the framework of galaxy and supermassive black hole (SMBH) co-evolution (Hopkins et al. 2008; Hickox & Alexander 2018; Lapi et al. 2018), star

Open Access article, published by EDP Sciences, under the terms of the Creative Commons Attribution License (https://creativecommons.org/licenses/by/4.0), which permits unrestricted use, distribution, and reproduction in any medium, provided the original work is properly cited.
This article is published in open access under the Subscribe to Open model. Subscribe to A&A to support open access publication.

formation, and SMBH accretion are likely co-occurring during an obscured phase. Radio emission provides a complementary probe of AGN activity along with X-ray emission. The radio band can identify dust-obscured sources where X-ray selection becomes increasingly incomplete, particularly in the Compton-thick regime. In addition, radio and X-ray observations only probe partially overlapping AGN populations, making radio data essential for a more complete census of AGN activity (Mazzolari et al. 2024). In particular, deep radio surveys ($S_{1.4\,\mathrm{GHz}} \leq 0.1$ mJy; e.g. Mancuso et al. 2017) are also sensitive to radio-quiet (RQ) AGNs, which exhibit evidence of nuclear activity in the X-ray, mid-infrared (MIR), or optical bands but show weak radio emission (i.e. no large-scale jets). The nature of radio emission within RQ AGN remains a subject of debate, since it likely arises from the interplay of multiple physical mechanisms, including compact jets on (sub-)kiloparsec scales, star-forming regions in the circumnuclear environment, and other AGN-driven processes such as coronal winds or radiatively driven shocks. This complexity highlights the diverse nature of RQ AGNs and suggests that their radio emission cannot be attributed to a single dominant mechanism (see Panessa et al. 2019 for a review; Bonato et al. 2017; Mancuso et al. 2017; Ceraj et al. 2018; Prandoni et al. 2018).

Most of the studies conducted so far on radio-selected optical–NIR dark sources have been based on deep, high-frequency surveys covering relatively small areas such as the Cosmic Evolution Survey (COSMOS; Scoville et al. 2007) and the Great Observatories Origins Deep Survey field in the northern hemisphere (GOODS-N, Dickinson et al. 2003; Giavalisco et al. 2004). Those include the *Karl G. Jansky* Very Large Array (VLA)-COSMOS 3 GHz Large Project (Smolčić et al. 2017; Talia et al. 2021; Behiri et al. 2023; Gentile et al. 2024, 2025), the ultra-deep 3 GHz VLA observations from the COSMOS-XS survey (van der Vlugt et al. 2021, 2022, 2023), and the 1.4 GHz VLA observations in the GOODS-N field (Owen 2018; Enia et al. 2022). Building on these previous efforts, our work aims to extend the study of radio-selected NIR dark sources to larger areas by exploiting the unique features of the Euclid Deep Field-North (EDF-N).

Covering approximately 22 deg^2, the EDF-N offers a significant increase in survey area, thus enabling the possibility to detect rare objects such as optical-NIR dark galaxies whose number density at $z > 3$ is estimated to be approximately 2×10^{-5} Mpc^{-3} (see e.g. Schreiber et al. 2018; Valentino et al. 2020; Gentile et al. 2024). Wide-area surveys are therefore crucial to efficiently identifying and statistically characterising these rare and extreme sources. In this work, we focused on the 10 deg^2 region covered by Low-Frequency Array (LOFAR) High Band Antenna (HBA) observations at 144 MHz, along with the available multi-wavelength information, including the Euclid Quick Release Q1 (2025) in the optical/NIR regime. This enables the exploration of the radio properties of these sources at much lower frequencies than typically used in past studies. The low-frequency regime is dominated by synchrotron emission, while the thermal free–free emission becomes negligible. Synchrotron self-absorption might, however, play an important role in suppressing the non-thermal emission (e.g. Mancuso et al. 2017; Schober et al. 2017).

The paper is organised as follows. In Sect. 2, we provide an overview of the multi-band data products used in this study. Sect. 3 describes the selection criteria, while Sect. 4 details the analysis methods. The main results are presented in Sect. 5, and finally, in Sect. 7, we discuss the implications of our findings and summarise our conclusions. Throughout the paper, we assume a Chabrier (2003) initial mass function (IMF) and consider a ΛCDM cosmology with $H_0 = 70\,\mathrm{km\,s^{-1}\,Mpc^{-1}}$, $\Omega_\Lambda = 0.7$, and $\Omega_\mathrm{m} = 0.3$. All magnitudes are reported in the AB system (Oke & Gunn 1983).

2. Data description

2.1. LOFAR multi-band catalogue

This paper is based on the radio source catalogue presented in Bisigello et al. (2025, B25 hereafter), which was produced based on an updated version of the LOFAR HBA radio source catalogue presented by Bondi et al. (2024), derived from 72 hours of observations in the EDF-N at the frequency $\nu = 144$ MHz. Images reach a spatial resolution of 6″ and a 1σ sensitivity of 32 μJy beam^{-1} over 10 deg^2. The catalogue includes radio sources with S/N > 5. The spurious fraction corresponds to around 3% for sources with $5.0 \leq$ S/N < 5.5, around ∼1.5% for sources with $5.5 \leq$ S/N < 6.0, and less than 0.5% for S/N > 10. B25 identified optical and/or MIR counterparts[1] by exploiting the optical catalogues from the Hawaii eROSITA Ecliptic Pole (HEROES, Taylor et al. 2023) survey, which reached 5σ depths of $g = 26.5$, $r = 26.2$, $i = 25.7$, $z = 25.1$, $y = 23.9$, NB816 = 24.4, and NB921 = 24.4, and from MIR *Spitzer* maps from the Cosmic Dawn Survey (Euclid Collaboration: Moneti et al. 2022; Euclid Collaboration: McPartland et al. 2025). B25 produced a new *Spitzer*/Infrared Array Camera (IRAC) source catalogue by performing a new source extraction aimed at maximising de-blending. Moreover, compared to the catalogue by Euclid Collaboration: Moneti et al. (2022), which only included the two shorter wavelength IRAC bands, the B25 catalogue combines the available observations in all four IRAC channels (3.6, 4.5, 5.8, and 8.0 μm), offering a more complete view of redder and potentially more obscured sources. Here we provide a summary of the extraction procedure, and we refer the reader to B25 for the detailed description. In brief, B25 exploited the `PHOTUTILS` Python package (Bradley et al. 2023) to create a segmentation map from the co-added 3.6 μm and 4.5 μm images, taking into account the respective error maps. They selected as sources all regions containing at least three connected pixels above three times the local RMS noise. A de-blending procedure was then applied, where peaks were identified as separate sources if they contained at least two pixels each above the flux threshold and exceeded a minimum contrast; the latter was defined as the fraction of the total source flux in the local peak. The contrast parameter ranges from zero (all local peaks treated as separate sources) to one (no de-blending); a very low contrast of 10^{-8} was chosen to maximise the de-blending capability[2]. This setup was fine-tuned by visually inspecting a subsample of potentially blended sources, confirming that individual extended sources were not erroneously split into multiple components. Finally, the segmentation map was used as a reference to each band separately to extract fluxes via aperture photometry. This approach allowed for the inclusion of objects detected only in the IRAC bands, which is particularly relevant for identifying redder, potentially more obscured counterparts to radio sources, as shown by previous studies (e.g., Williams et al. 2019b).

Additionally, B25 included the *u* band observations that are also part of the Cosmic Dawn Survey (Euclid Collaboration:

[1] In B25, the regime covered by *Spitzer* bands is defined as the NIR. In this paper, we refer to this wavelength range as MIR instead.

[2] We verified that the number of de-blended sources remained unchanged for contrast values between 10^{-4} and 10^{-8}, and a visual inspection confirmed that no over-segmentation was introduced.

McPartland et al. 2025). Counterpart identification was carried out using a likelihood-ratio method (de Ruiter et al. 1977; Sutherland & Saunders 1992), complemented by visual inspection. This combined approach enabled the reliable identification of both isolated and compact radio sources, as well as those with complex or extended morphologies, including those in crowded fields. B25 also exploited LOFAR intermediate-resolution data (1.″5) obtained with the International LOFAR Telescope (ILT), including the international LOFAR stations. These observations cover an inner region of the EDF-N of 2.5 deg × 2.5 deg and combine 32 of the available 72 hours, reaching a central RMS noise of 36 μJy beam^{-1}; they were used to improve the accuracy of previous radio positions. As a result of their analysis, 99.2% of the radio sources were associated with a reliable optical and/or MIR counterpart, corresponding to 19 401 out of 19 550 objects. Moreover, the B25 catalogue also includes FIR data obtained by cross-matching the LOFAR sources with photometry from the *Herschel* Space Observatory, which were retrieved from the IPAC infrared science archive. Specifically, LOFAR sources were searched for counterparts in the Photodetector Array Camera and Spectrometer (PACS) Point Source Catalogue (Marton et al. 2017) at 70, 100, and 160 μm, and in the Spectral and Photometric Imaging Receiver (SPIRE) Point Source Catalogue (Schulz et al. 2018) at 250, 350, and 500 μm. A matching radius of 6″ was adopted for PACS, and 12″ for SPIRE. As a result of this cross-match, approximately 20% of the LOFAR sources have FIR detections in at least one of the *Herschel*/SPIRE bands. In Sect. 4.1 we describe the analysis of FIR data and the cross-matching performed specifically for our sample. In the following sections, we describe the additional datasets used in this paper, whose properties are summarised in Table 1.

2.2. Euclid optical and NIR data

The *Euclid* mission (see Euclid Collaboration: Mellier et al. 2025 for an overview) will provide high-resolution optical imaging, as well as NIR imaging and spectroscopy, over about 14 000 deg^2 of extragalactic sky. The first set of data was released on March 19, 2025 (Quick Release 1 or Q1). A detailed description of the Q1 data release is provided by Euclid Collaboration: Aussel et al. (2026). Data products and processing from the Visible Camera (VIS) and Near-Infrared Spectrometer and Photometer (NISP) are reported in Euclid Collaboration: McCracken et al. (2026) and Euclid Collaboration: Polenta et al. (2026), respectively. The VIS instrument observes in the visible (I_E, Euclid Collaboration: Cropper et al. 2025), while NISP includes three NIR filters (Y_E, J_E, and H_E band, see Euclid Collaboration: Jahnke et al. 2025). The photometric catalogue is presented in Euclid Collaboration: Romelli et al. (2026). The EDF-N is covered by Q1 observations over 22.9 deg^2 in all four photometric bands. Ground-based data products have also been included along with *Euclid* bands. In this work, we exploited images from the Ultraviolet Near-Infrared Optical Northern Survey (UNIONS, Gwyn et al. 2025), in particular observations from the Subaru Telescope Hyper Suprime Cam (HSC) and the Canada-France-Hawaii Telescope (CFHT), ranging between 0.3 μm and 0.9 μm. The complete list of filters available in each field, with their effective wavelengths, their corresponding observational depths, full widths at half maximum (FWHMs), and area coverage is reported in Table 1.

2.3. Mid-IR data

Along with the *Spitzer*/IRAC photometry described in Section 2.1, we exploited *Spitzer*/MIPS mosaics available in the North Ecliptic Pole (NEP), which covers a limited area of 0.4 deg^2 (Jarrett et al. 2011) and is part of the Spitzer Enhanced Imaging Products (SEIP). The Wide-field Infrared Survey Explorer (WISE; Wright et al. 2010) provides additional MIR coverage over the full sky. In this work, we also exploited data from the AllWISE and unWISE programmes. AllWISE combines data from the WISE cryogenic and NEOWISE (Mainzer et al. 2011) post-cryogenic missions and includes both a source catalogue and an image atlas in four photometric bands–$W1$, $W2$, $W3$, and $W4$–centred at 3.4, 4.6, 12, and 22 μm. The unWISE products (Lang 2014) collect co-added WISE images that have not been blurred and retain the intrinsic resolution of the data. Since the first two bands overlap with and are shallower than IRAC1 and IRAC2, we focused on WISE $W3$ and $W4$ (12 μm and 22 μm) to complement the IRAC photometry.

Table 1. Filters used in this work, with their associated effective wavelengths, observed depths, FWHMs, and area of the EDF-N covered.

Band	$\lambda_{\rm eff}$ (μm)	Depth	FWHM (arcsec)	Area (deg^2)
CFHT/MegaCam u	0.372	24.2 mag	0.89	13.7
HSC g	0.480	25.7 mag	0.90	5.4
CFHT/MegaCam r	0.640	24.8 mag	0.71	13.7
Euclid VIS/I_E	0.715	25.45 mag	0.16	22.9
HSC z	0.891	24.1 mag	0.71	5.4
Euclid NISP/Y_E	1080.9	24.6 mag	0.3	22.9
Euclid NISP/J_E	1367.3	24.1 mag	0.3	22.9
Euclid NISP/H_E	1771.4	23.9 mag	0.3	22.9
Spitzer/IRAC1	3.550	24.8 mag	1.66–1.95[a]	11.74
Spitzer/IRAC2	4.493	24.8 mag	1.72–2.02[a]	11.54
Spitzer/IRAC3	5.696	20.8 mag	1.88	0.61
Spitzer/IRAC4	7.799	21.9 mag	1.98	0.62
WISE $W3$	12.082	19.1 mag	8.5	All sky
WISE $W4$	22.194	17.2 mag	17	All sky
Spitzer/MIPS24	23.7	16.95 mag	6	0.4
AKARI/FIS65	65	3.2 Jy	37	All sky
AKARI/FIS90	90	0.55 Jy	39	All sky
AKARI/FIS140	140	3.8 Jy	58	All sky
AKARI/FIS160	160	7.5 Jy	61	All sky
Herschel/SPIRE250	250	4.5×10^{-2} Jy	18.2	16.05
Herschel/SPIRE350	350	3.8×10^{-2} Jy	24.9	16.05
Herschel/SPIRE500	500	5.4×10^{-2} Jy	36.3	16.05
JCMT/SCUBA-2	850	$(5–11.5) \times 10^{-3}$ Jy	14.6	2.0

Notes. Reported magnitudes are the 5σ observed depths. Optical and *Euclid* magnitudes were computed adopting a 2 × FWHM diameter aperture and correspond to the median depths of the observing tiles (Euclid Collaboration: Romelli et al. 2026). IRAC1 and IRAC2 depths refer to average values in the fields derived considering 2″ empty apertures (see Euclid Collaboration: Moneti et al. 2022 and Euclid Collaboration: McPartland et al. 2025). IRAC3 and IRAC4 depths were derived from B25 by averaging depths derived from the catalogue after correcting from aperture to total magnitudes. AKARI depths refer to the 5σ noise level per scan in the normal mode (see Kawada et al. 2007). [a] Numbers refer to the cryogenic and warm missions, respectively.

2.4. Far-IR data

We made use of multiple FIR and sub-millimetre (mm) data products in the North Ecliptic Pole (NEP) field. First, we included the AKARI/Far Infrared Surveyor (FIS) All-Sky Survey Bright Source Catalogue (Yamamura et al. 2009) derived

from the AKARI Far-infrared All-Sky Survey (Doi et al. 2015), which provides observations at 65, 90, 140, and 160 μm over the NEP. In addition to the PACS and SPIRE point-source catalogues used in B25, we utilised the products available from the *Herschel* Extragalactic Legacy Project (HELP; Shirley et al. 2019, 2021), including SPIRE maps and blind catalogues from the *Herschel*-AKARI NEP Deep Survey covering 9.2 deg^2 (Pearson et al. 2017a). Finally, we made use of data from the James Clerk Maxwell Telescope (JCMT) SCUBA-2, and particularly from the North Ecliptic Pole SCUBA-2 (NEPSC2) 850 μm survey (Shim et al. 2020), covering over 2 deg^2 of the NEP.

2.5. LOFAR ILT 0.″3 data

We then exploited recent ILT LOFAR imaging at sub-arcsecond resolution (0.″3) to investigate the nature of the radio emission of our sources. The map covers the inner 2.5 deg × 2.5 deg of the EDF-N, reaching a central sensitivity of 32 μJy beam^{-1}. The wide-field image and the radio catalogue associated with these data will be presented in a future paper (Bondi et al., in prep.). At 144 MHz, the sub-arcsecond resolution achieved by LOFAR ILT is sensitive to compact radio emission associated with AGNs (see e.g. Morabito et al. 2022, 2025a) and, as discussed throughout this work, provides a key diagnostic to identify AGN activity in our sources.

3. Sample selection

Our selection started from a subsample of the B25 catalogue, denominated 'IRAC-only' sources. This sample comprises 1363 objects, corresponding to approximately 7% of the total number of LOFAR sources, and results from the B25 cross-matching procedure. It is composed of sources that lack a reliable counterpart in the optical bands of the HEROES catalogue and have a counterpart in the IRAC bands instead. Among these sources, although undetected in the optical bands of the HEROES catalogue (g, r, i, z, y), B25 identified 218 with a counterpart in the u band of the Cosmic Dawn Catalogue. They suggested that this could indicate that some IRAC-only sources lie near the sensitivity limit of the optical data, where more advanced extraction techniques might recover faint optical fluxes. Furthermore, B25 found 94 spurious associations via visual inspection, largely caused by IRAC blending or by the over-segmentation of extended nearby galaxies. This latter issue arises from the optical catalogue's source extraction setup, which favours compact sources and may erroneously split a single large galaxy into multiple components, leading to incorrect cross-matches. Thus, we removed the above-mentioned objects from our starting sample of IRAC-only sources, obtaining a total of 1051 IRAC-only radio sources.

3.1. Cross-matching and visual inspection of Euclid Q1 products

In addition to the visual inspection conducted in B25, we analysed the remaining 1051 IRAC-only radio sources (cleaned IRAC-only sample) exploiting *Euclid* Q1 data products. We proceeded as follows:

– We overlapped *Euclid*, LOFAR, and IRAC positions and the respective 3 and 5σ contours to *Euclid* VIS and NISP maps. We then excluded all the sources whose LOFAR 1.″5 and/or IRAC2 emission at 5σ contained a 5σ NIR source corresponding to the radio and MIR centroid, if present, in at least one of the *Euclid* bands. In other words, following a similar approach to that applied by Talia et al. (2021) and Behiri et al. (2023), our sample only includes sources without a clear 5σ *Euclid* detection corresponding to the radio/IRAC source. As a result of this initial step, a total of 304 candidate dark sources were identified;
– Second, we cross-matched both IRAC and radio positions of this sample with sources in the *Euclid* catalogue. We selected a matching radius of 0.″9, corresponding to around 3× the average positional error of LOFAR positions, which is the instrument with the lowest angular resolution. We chose to match both LOFAR and IRAC positions to *Euclid* independently, given that in some cases the separation between LOFAR low-resolution and IRAC coordinates can be large (e.g. above 1″ for 50/304 sources in our sample), and multiple NIR counterparts might be found within the IRAC or LOFAR beams. As a result of this cross-match, we obtained 164 objects without and 140 with a counterpart in the *Euclid* catalogue. Among the sources with a *Euclid* counterpart, nine are flagged as spurious in the catalogue (`SPURIOUS_FLAG=1`). We did not include these objects in our sample, since their association with radio and/or MIR emission suggests that they may correspond to real sources rather than artefacts;
– We then performed a second visual inspection. In this step, we carefully checked the remaining 131 sources with a *Euclid* counterpart to verify that the NIR coordinate was correctly associated with the same radio/MIR position. At the same time, for the sources without a *Euclid* counterpart, we inspected the images to ensure that there was no significant emission (above 3σ) in the vicinity of the IRAC/radio centroid. We found only two cases in which the radio and/or MIR positions are associated with different NIR counterparts, corresponding to objects whose NIR position was wrongly cross-matched with the IRAC2 or LOFAR (low resolution) one because of blending. These sources can therefore be considered *Euclid* 'dark' (E-dark hereafter) and were added to the sample of objects without a counterpart in the *Euclid* catalogue.

To summarise, with the above selection, we found a sample of 166 E-dark LOFAR-selected targets. We found no evidence of strong gravitational lensing among our sources.

3.2. Selection of the 'isolated' sample

Starting from the parent sample of 166 E-dark radio-selected (RS) targets described in the previous section, we define a subsample, hereafter referred to as the 'isolated' sample. This subset is specifically tailored to our preliminary analysis as it minimises the contamination from nearby objects, at least up to IRAC2, allowing for a cleaner interpretation of their properties. The isolated sample consists of all the E-dark targets whose MIR/radio emission contours at 3σ from IRAC2, or the LOFAR intermediate-resolution map when available, do not overlap with the 3σ NIR/MIR emission of nearby IRAC2 or *Euclid* sources. This criterion removed about 30% of the sources inside the sample of 166 objects. Moreover, we excluded sources with an evident MIR or radio blending (corresponding to approximately 11% of the E-dark sample), located near an extended bright local source or a spike originating from a nearby star (around 5% of the E-dark sample). From visual inspection, we collected a sample of 88 isolated E-dark sources. In Fig. 1, we show examples of four such E-dark sources according to our classification criteria, including a representative isolated source that meets the

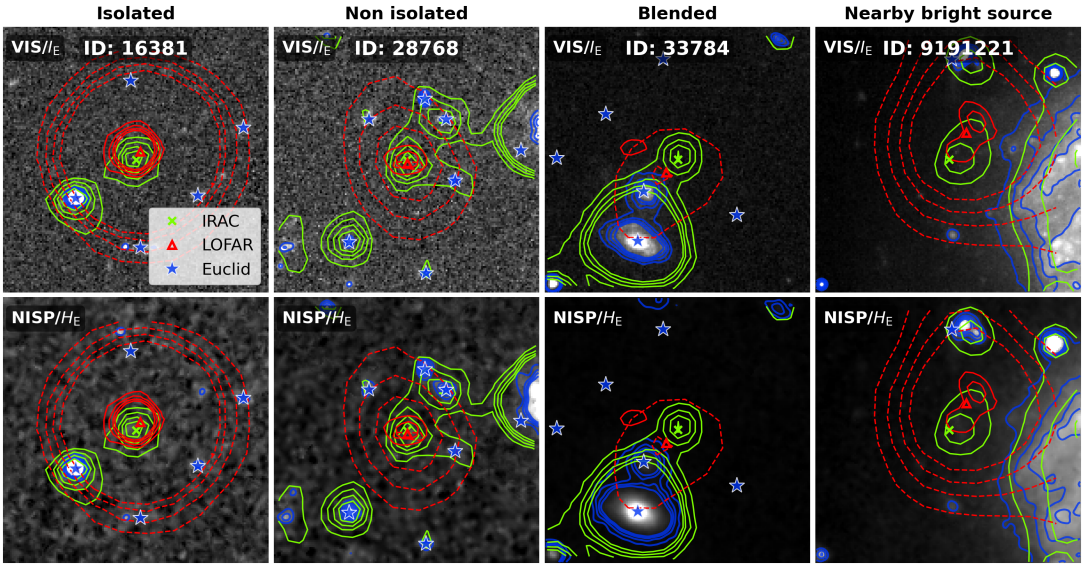


Fig. 1. Examples of four E-dark sources illustrating the classification used in this work: isolated sources (satisfying the criteria described in Sect. 3.2), non-isolated sources, blended sources, and sources affected by a nearby bright object. Cutouts display the VIS I_E (top panels) and NISP H_E (bottom panels) images centred at the MIR position of the sources in our sample. The blue, green, and red contours represent the 3σ, 5σ, 7σ, and 9σ emission from *Euclid*, IRAC2, and LOFAR, respectively, where for LOFAR the intermediate-resolution emission is shown with solid contours and the low-resolution emission with dashed contours. The centroid of the emission on each instrument is shown, in the corresponding colour, with stars, crosses, and triangles for *Euclid*, IRAC2, and LOFAR. The ID of the object matches the one listed in the B25 catalogue. Postage stamps are $15'' \times 15''$.

Table 2. Summary of sample-selection steps described in Sect. 3.

Selection step	Number of sources
IRAC-only cleaned (B25)	1051
Visual inspection	304
Euclid catalogue cross-match	164
Visual inspection, *Euclid* mismatch	2
Total E-Dark	166
Isolated E-Dark	88

conditions described above. In Table 2 we summarise the main steps described in this section.

The sources in the isolated sample span a flux-density range of $0.15\,\mathrm{mJy} \leq S_{144\,\mathrm{MHz}} \leq 50\,\mathrm{mJy}$. However, the vast majority of them (about 93%) have $S_{144\,\mathrm{MHz}} \leq 2\,\mathrm{mJy}$. This flux regime falls into the region of the radio differential number counts where SFGs and RQ AGN begin to dominate over the radio-loud AGN population (e.g., Mancuso et al. 2017).

4. Analysis

4.1. Photometric counterparts of isolated E-dark sources

Besides the photometry available from the B25 catalogue, we made use of data described in Sect. 2 to enrich the available photometric information of the sample of isolated E-dark sources. For optical/NIR bands (i.e. u, g, r, z, I_E, Y_E, J_E, and H_E) no source is detected by definition, and we derived a 3σ upper limit by measuring the flux inside approximately 100 random apertures in a $30'' \times 30''$ cutout, avoiding bright sources, and then computing their standard deviation. In the MIR, besides the IRAC1 and IRAC2 detections, five (three) objects have counterparts in IRAC3 (IRAC4), while 16 sources are covered by MIPS observations, showing no counterpart. For the latter sources, we computed 3σ upper limits as described above.

We manually extracted WISE fluxes at IRAC positions by adopting `PHOTUTILS` and by following the procedure reported in the Explanatory Supplement to the AllWISE Data Release Products[3]. We performed aperture photometry using the fixed circular apertures and relative correction factors reported in Section 4.2 of the Explanatory Supplement to the WISE All-Sky Data Release Products[4]. For background estimation, we used a standard annulus with inner and outer radii of $50''$ and $70''$, respectively, similarly to the values adopted in the AllWISE source catalogue, and masking pixels above the 3σ noise level. We found, respectively, two and three detections for WISE3 and WISE 4. Upper limits for the remaining targets were computed in a $400'' \times 400''$ cutout. For AKARI, there are no individual detections from the AKARI/FIS All-Sky Survey Bright Source Catalogue; therefore, we computed the upper limits from the 3σ rms of the individual $900'' \times 900''$ cutouts centred at the source's position.

For SPIRE, we followed the approach described in Wang et al. (2021). We first cross-matched our isolated E-dark sources and the HELP blind catalogues (Shirley et al. 2021). Initially, we adopted a search radius of $6''$. For sources with a match within this radius, we then repeated the cross-matching using a radius of $18''$, corresponding to the FWHM of the SPIRE 250 µm beam. If the matches were unique, the fluxes from the blind photometry catalogues were adopted for further analysis. For sources with multiple possible counterparts within the SPIRE beam, we assigned the SPIRE fluxes using the probabilistic de-blending tool `XID+` (Hurley 2017; Pearson et al. 2017b, 2018), applied to regions around the LOFAR sources on the SPIRE maps. We refer

[3] https://wise2.ipac.caltech.edu/docs/release/allwise/expsup/index.html
[4] https://wise2.ipac.caltech.edu/docs/release/allsky/expsup/index.html

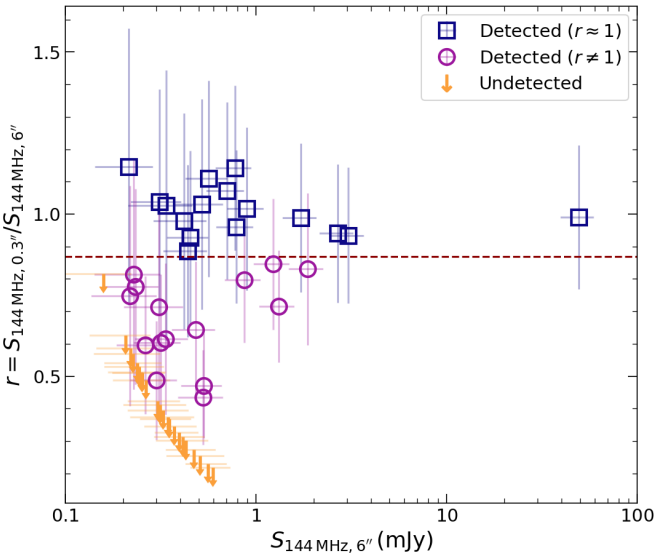


Fig. 2. Ratio between 144 MHz LOFAR fluxes at high (0.″3) and low (6″) resolution versus the 144 MHz LOFAR flux at 6″. The horizontal dashed red line is shown as a reference for the aperture flux ratio consistent with unity (represented with blue squares) within the flux uncertainties, corresponding to approximately 15% of the LOFAR flux at 6″. Sources detected in the LOFAR ILT image are highlighted in blue and purple, corresponding to flux ratios consistent and not consistent with unity, respectively. Yellow arrows mark the 3σ upper limits for the 22 sources without a detection in the LOFAR ILT map.

the reader to Wang et al. (2021) for further details of this procedure. Combining this photometry with the SPIRE point-source catalogue, we obtained 17, 20, and 16 detections at 250, 350, and 500 μm, respectively. We also note that no PACS counterparts are available for our sample from the cross-matching performed in B25. Finally, we cross-matched the 88 isolated E-dark objects with the NEPSC2 catalogue, adopting a search radius of 15″, which corresponds to the effective beam FWHM of SCUBA-2 at 850 μm, finding two counterparts.

4.2. Compact radio emission in the ILT-LOFAR subsample

We searched for counterparts in the LOFAR ILT map at a 0.″3 resolution. Among the 88 sources, 50 are covered by the central 1.25 deg × 1.25 deg region, reaching the highest sensitivity. We searched for counterparts within 1″ of the IRAC position, finding 28 sources with S/N > 4. The remaining 22 objects were not detected at 0.″3. Moreover, we also searched for additional counterparts in the least sensitive regions of the 0.″3 radio map, where the rms noise reaches 64 μJy beam^{-1}. We found three sources in this area, all with S/N > 5. Source sizes were obtained by fitting a single Gaussian component to the brightness distribution at 0.″3 resolution of the detected E-dark galaxies. Most of the detections are consistent with a point-like morphology, with a few exceptions (i.e. ID 17587, 12515, 9319351, 27761), which show a multi-component morphology in the high- and intermediate-resolution LOFAR maps.

A first indication of the nature of the radio emission can be obtained by comparing the high- and low-resolution LOFAR flux densities. In Fig. 2, we show the ratio, r, between the 0.″3 and 6″ radio fluxes as a function of the 6″ flux density. Out of the 53 sources covered by the LOFAR ILT high-resolution image, 16 display flux ratios consistent with unity within the uncertainty on the radio flux at 6″ (corresponding to ratios greater than 0.87). This suggests a dominant radio component and, therefore, that a significant fraction of the radio emission is concentrated on sub-arcsecond scales. For 15 objects, the ratio is lower than 0.87, indicating that part of the extended emission is lost at higher angular scales. In these cases, the radio emission could originate from both AGN and star formation processes. For the remaining 22 sources without a detection at 0.″3, we show 3σ upper limits, suggesting that their radio emission is likely dominated by star formation rather than by an AGN. While this information alone is not sufficient to firmly establish or exclude the presence of AGN activity, it motivates a more quantitative analysis of the compact radio emission and provides useful constraints for the radio component of the spectral-energy-distribution (SED) fitting for these sources, as discussed in the following section.

As introduced in the previous section, LOFAR ILT 0.″3 data can be exploited to search for compact emission associated with AGN activity by measuring the radio-brightness temperature T_b. Radio emission in SFGs is expected to have an upper limit in surface brightness (Condon et al. 2002), meaning that values surpassing this threshold can only be produced by AGN-related processes. The brightness temperature scales as $T_b \propto \nu^{-2}\theta^{-2}$, where ν is the observing frequency and θ is the angular resolution. At low frequencies, such as 144 MHz, sub-arcsecond-resolution observations (0.″3, corresponding to approximately 2 kpc at a reference redshift of $z = 3$) have proven to be sufficient to provide reliable T_b measurements (Morabito et al. 2022). Moreover, this approach can be exploited to probe AGN activity even in sources that do not show a clear radio excess relative to the SFR (Morabito et al. 2025b). Since the estimation of T_b requires knowledge of the source redshift, we combined the radio measurements with SED fitting to derive the physical properties of the sample.

4.3. SED fitting

We modelled the SED of our sample using the Code Investigating GAlaxy Emission (`CIGALE`; Boquien et al. 2019). `CIGALE` is a Python SED-fitting code able to reproduce broadband UV-to-radio photometric data according to the energy balance (i.e. the energy absorbed from the stellar UV-to-NIR emission is the same as the one re-emitted by the dust in the MIR and FIR regimes). `CIGALE` estimates the physical properties by comparing modelled galaxy SEDs, generated from a user-defined grid of input parameters, to observed ones. For each parameter, a probability distribution function (PDF) was constructed based on a χ^2 comparison of the observed SED with all models in the n-dimensional grid. The output values include the 'best' model, corresponding to the minimum χ^2 point, and the Bayesian-like estimates, obtained as the likelihood-weighted mean of the PDF. The associated uncertainties were computed as the likelihood-weighted standard deviation. The stellar emission was computed following the Bruzual & Charlot (2003) population synthesis models, associated with a Chabrier (2003) IMF and metallicity value of $Z = 0.02$. We tested additional values for the metallicity (i.e. $Z = 0.008$ and $Z = 0.05$), finding no significant differences in the derived physical properties. We also included the nebular emission model based on Inoue (2011) templates, using the standard values provided by `CIGALE`. We assumed a delayed star formation history (SFH) with a main star formation episode and an optional burst/quench, quantified by the parameter t_{bq} (i.e. the age of the burst/quench episode). The SFR evolves as

$$\mathrm{SFR}(t) \propto \frac{t}{\tau^2}\,\exp\left(-\frac{t}{\tau}\right), \tag{1}$$

Table 3. CIGALE modules and relative parameters used in this work. Parameters not explicitly listed are fixed to the default values set by CIGALE.

Module	Parameter	Description	Values
SFH (Delayed)	τ	Stellar e-folding time	500, 1000, 5000 Myr
	t	Stellar age	500, 1000, 3000, 5000 Myr
	$t_{\rm bq}$	Burst/quench age	1, 10, 100, 300 Myr
	$r_{\rm SFR}$	Ratio of SFR after/before $t_{\rm bq}$	0.1, 1, 10
Dust attenuation (mod. Charlot & Fall 2000)	$A_{V,\,\rm ISM}$	ISM V-band attenuation	0.3, 2.5, 4.5, 6.5
	Slope BC	Power law slope of the attenuation in the birth clouds	−0.7
Dust emission (Dale et al. 2014)	$\alpha_{\rm d}$	Slope	1, 1.5, 2, 3, 4
AGN (Fritz et al. 2006)	$\tau_{\rm AGN}$	Optical depth	1.0
	Ψ	Angle between equator and line of sight	0.001, 50.1, 89.99 deg
	$f_{\rm AGN}$	AGN fraction	0.0, 0.1, 0.3, 0.5, 0.7, 0.99
	$\lambda_{\rm fracAGN}$	Wavelength range to compute $f_{\rm AGN}$	0.1–7175.6 µm
Radio	$q_{\rm IR}$	IR/radio correlation	2.2, 2.5, 2.8
	$R_{\rm AGN}^{(\dagger)}$	Radio-loudness parameter	0.0, 0.5, 1, 5, 10/10, 100, 1000
	$\alpha_{\rm SF}$	Radio spectral slope for SF	−0.7
	$\alpha_{\rm AGN}$	Radio spectral slope for AGN	−0.8
Redshift	z	...	0.0–6.0 (step = 0.2)

Notes. $^{(\dagger)}$ The set of $R_{\rm AGN}$ values depends on the sample used (see Sect. 4.3 for details).

where t is the cosmic time and τ is the time at which the SFR peaks.

We modelled the dust attenuation in the far-UV–optical regime using the modified approach of Charlot & Fall (2000), which introduces an age-dependent attenuation described by two separate power laws: one for the diffuse interstellar medium (ISM) and one for the stellar birth clouds (BCs). Both components assume a fixed attenuation slope of $\mathrm{d}A_\lambda/\mathrm{d}\lambda = -0.7$, and the V-band attenuation was computed as

$$\mu = \frac{A_V^{\rm ISM}}{A_V^{\rm ISM} + A_V^{\rm BC}}. \tag{2}$$

We assumed $A_V^{\rm ISM} \in [0.5, 6.0]$ and the default value of $\mu = 0.44$. Dust emission was modelled using the Dale et al. (2014) templates, parametrised by the $\alpha_{\rm d}$ parameter defined as $\mathrm{d}M_{\rm d}(U) \propto U^{-\alpha_{\rm d}}\,\mathrm{d}U$, where $M_{\rm d}$ is the dust mass and U the intensity of the radiation field. The AGN contribution to the total galaxy luminosity (UV-to-radio) was taken into account assuming the templates from Fritz et al. (2006). By specifying a wavelength range in the parameter $\lambda_{\rm fracAGN}$, it is possible to account for all the components in the computation of the AGN fraction (Yang et al. 2022), which is defined as

$$f_{\rm AGN} = \frac{L_{\rm AGN}}{L_{\rm AGN} + L_{\rm galaxy}}, \tag{3}$$

where $L_{\rm AGN}$ and $L_{\rm galaxy}$ are integrated from the UV- to the FIR regime (0.1–7175.6 µm). The parameter $f_{\rm AGN}$ was set to vary in a grid of values: 0.0, 0.1, 0.3, 0.5, 0.7, and 0.99. In the latest version of CIGALE (Yang et al. 2022), the modelling of the radio emission was separated into two components: one originating from star formation and one from the AGN. The former was derived from the IR/radio correlation parameter ($q_{\rm IR}$, Helou et al. 1985; Condon et al. 2002; Yun et al. 2001), for which we adopted input values of 2.2, 2.5, and 2.8. The latter was computed via the radio-loudness parameter $R_{\rm AGN} = L_{\nu,\,5\,\rm GHz}/L_{\nu,\,2500\,\text{Å}}$, where $L_{\nu,\,5\,\rm GHz}$ and $L_{\nu,\,2500\,\text{Å}}$ are the monochromatic AGN rest-frame luminosities at 5 GHz and 2500 Å, respectively. For sources with a radio-flux ratio of $r \approx 1$ (see Fig. 2), we adopted $R_{\rm AGN} = 10, 100, 1000$, while for the remaining sources we used $R_{\rm AGN} = 0.0, 0.5, 1.0, 5.0, 10.0$. For the remaining 35/88 sources without coverage in the ILT LOFAR observations, we have no prior information on the nature of the radio emission. Therefore, we repeated the SED-fitting procedure allowing the radio-loudness parameter to vary over the full range of $R_{\rm AGN} = 0.0$–1000. However, in the absence of high-resolution radio data, the constraints on these sources are more uncertain, and no estimates of the radio-brightness temperature could be obtained. In the CIGALE setup, we included a 10% uncertainty on the fluxes, added in quadrature. In Table 3 we summarise the input parameters adopted in our analysis.

5. Physical properties of individual sources

In this section, we describe the main physical properties derived from the SED fitting. We stress that, due to the reduced photometric coverage, these properties are subject to large uncertainties. This holds in particular for sources without counterparts in the FIR. For this reason, when presenting and discussing our results we primarily focus on sources with at least one detection in the SPIRE or SCUBA-2 bands, where relevant, while the results for the remaining objects are used mainly as indicative reference values. The resulting best-fit SEDs for the objects with at least one FIR detection are reported in Appendix A for the 53/88 sources covered by LOFAR ILT high-resolution map, while the results for the remaining 35/88 targets are shown in Appendix B. The catalogue containing the physical properties described in this section is publicly available as additional material for this paper.

In Fig. 3, we show the photometric redshift and 144 MHz luminosity distributions for the individual sources in our sample of isolated E-dark sources. For comparison, we also report the redshift values for the entire parent sample of LOFAR

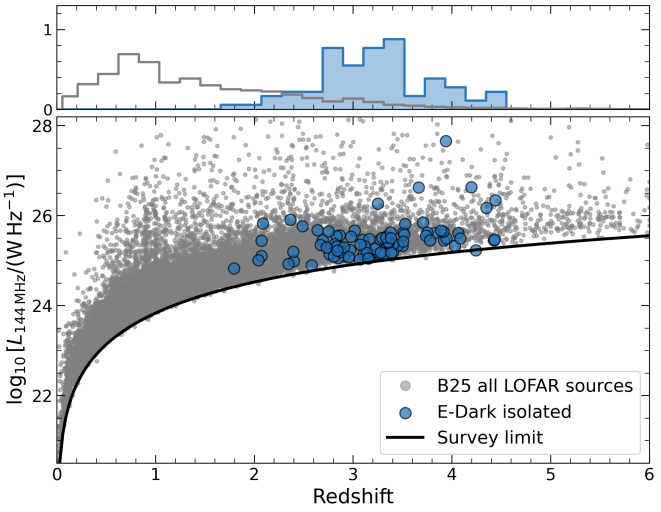


Fig. 3. Radio luminosity of 88 isolated E-dark sources (blue) as a function of redshift. In grey we show the parent sample of LOFAR sources presented in B25. Distributions plotted in the upper panel were normalised to the total number of sources in each sample.

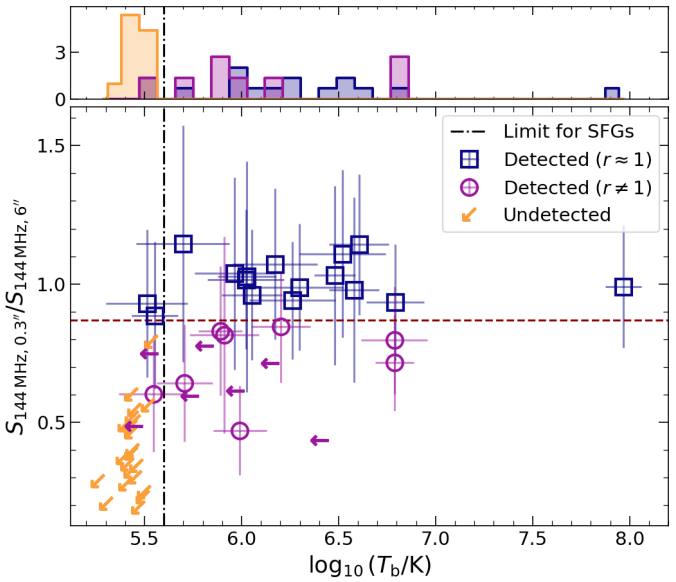


Fig. 4. Ratio between 144 MHz LOFAR fluxes at high (0.″3) and low (6″) resolution versus the brightness temperature. The vertical dash-dotted line represents the threshold adopted to distinguish between radio emission originating from star formation and AGN processes. Arrows mark 3σ upper limits for sources with either no detection in the LOFAR ILT map at 0.″3 or with an unreliable measure of the Gaussian components.

sources described in B25. Our sources span a luminosity range of $24.82 \leq \log_{10}[L_{144\,\mathrm{MHz}}/(\mathrm{W\,Hz^{-1}})] \leq 27.65$.

The redshift distribution spans $1.8 \lesssim z \lesssim 4.4$, with a mean weighted value of $\langle z \rangle = 3.4$ and a weighted standard deviation of $\sigma_z = 0.6$. All the objects of our sample were fitted with a reduced $\chi^2 < 1.1$. Nine sources belong to the high-z tail of the distribution, with a photometric redshift of >4.0. The derived photometric redshifts of our sample are in good agreement with median values obtained from similar samples of optical/NIR dark radio-selected sources (e.g. $z_{\mathrm{ph}} = 3.1$; Talia et al. 2021).

We computed the brightness temperature as

$$T_{\mathrm{b}} = 1.22 \times 10^6\,(1+z)\left(\frac{\nu}{1\,\mathrm{GHz}}\right)^{-2}\left(\frac{\theta_{\mathrm{maj}}\theta_{\mathrm{min}}}{1\,\mathrm{arcsec}^2}\right)^{-1}\left(\frac{S_{\mathrm{T}}}{1\,\mathrm{Jy}}\right)\mathrm{K}, \quad (4)$$

where ν is the observed frequency (here 144 MHz) and S_{T} is the corresponding total flux density. θ_{min} and θ_{maj} are the deconvolved major and minor axes of the fitted elliptical Gaussian components. The maximum brightness temperature attainable by a starburst galaxy, $T_{\mathrm{b}}^{\mathrm{SF}}$, was given by Condon et al. (1991) as

$$T_{\mathrm{b}}^{\mathrm{SF}} \leq T_e\left[1 + 10\left(\frac{\upsilon}{1\,\mathrm{GHz}}\right)^{0.1-\alpha}\right]. \quad (5)$$

In the above expression, T_{e} is the thermal electron temperature, here assumed to be approximately 10^4 K, and α is the radio spectral index. In Fig. 4 we report the flux ratio, r, as a function of the inferred T_{b}. $T_{\mathrm{b}}^{\mathrm{SF}}$ was computed as the spectral index value of $\alpha = -0.8$, corresponding to $\log_{10}(T_{\mathrm{b}}^{\mathrm{SF}}/\mathrm{K}) = 5.6$. We also report 3σ upper limits for sources with either no detection in the LOFAR ILT map at 0.″3 or with an unreliable fit of the Gaussian component to the brightness distribution. All the 22 sources not detected at 0.″3 (highlighted in yellow in Fig. 4) show $\log_{10}(T_{\mathrm{b}}/\mathrm{K}) < 5.6$, suggesting that the radio emission in these galaxies is likely to be dominated by star formation processes. Of the 16 sources with $r \approx 1$, all but three have $\log_{10}(T_{\mathrm{b}}/\mathrm{K}) > 5.6$, which is consistent (within their uncertainties) with AGN-dominated radio emission. Of the remaining three sources, two lie below the threshold but are compatible with being above it within their error, while the third lies slightly above the threshold but is also compatible with being below it once uncertainties are taken into account. For the remaining 15 objects detected with $r \neq 1$, seven have upper limits on the brightness temperature, two of which lie below $\log_{10}(T_{\mathrm{b}}/\mathrm{K}) = 5.6$, while all but two of the remaining sources have $\log_{10}(T_{\mathrm{b}}/\mathrm{K}) > 5.6$. The two exceptions lie on opposite sides of the threshold but are consistent with crossing it within their uncertainties. This result suggests that the radio emission in this subsample may originate from both AGN activity and star formation.

To estimate the possible radio excess, we derived the IR/radio correlation (IRRC) parameter q_{IR}, which is computed as (Bell 2003; Ivison et al. 2010a,b; Sargent et al. 2010)

$$q_{\mathrm{IR}} = \log_{10}\left(\frac{L_{\mathrm{IR}}}{3.75 \times 10^{12}\,\mathrm{W\,Hz^{-1}}}\right) - \log_{10}\left(\frac{L_{1.4\,\mathrm{GHz}}}{\mathrm{W\,Hz^{-1}}}\right). \quad (6)$$

In the above expression $L_{1.4\,\mathrm{GHz}}$ is the rest-frame total (i.e. including possible AGN emission) radio luminosity computed from the 144 MHz flux density and the photometric redshift, assuming a power-law spectrum for the radio emission $S_\nu \propto \nu^\alpha$, where $\alpha = -0.7$ (Novak et al. 2017). L_{IR} is the rest-frame FIR luminosity originated by star formation and defined in the 8–1000 μm range. The AGN fraction inferred from the SED fitting is subject to large uncertainties due to the poor photometric coverage in the MIR. Therefore, we followed G25 and estimated an AGN fraction according to the distance of our sources from the IRRC, hereafter denoted as $f_{\mathrm{AGN,\,REX}}$ to indicate the radio excess. For this purpose, we adopted the parametrisation of Delhaize et al. (2017):

$$q_{\mathrm{IR}} = (2.88 \pm 0.03)\,(1+z)^{-0.19\pm0.01}, \quad (7)$$

from which we computed the AGN fraction, defined as

$$f_{\mathrm{AGN,\,REX}} = 10^{q-\tilde{q}(z)}. \quad (8)$$

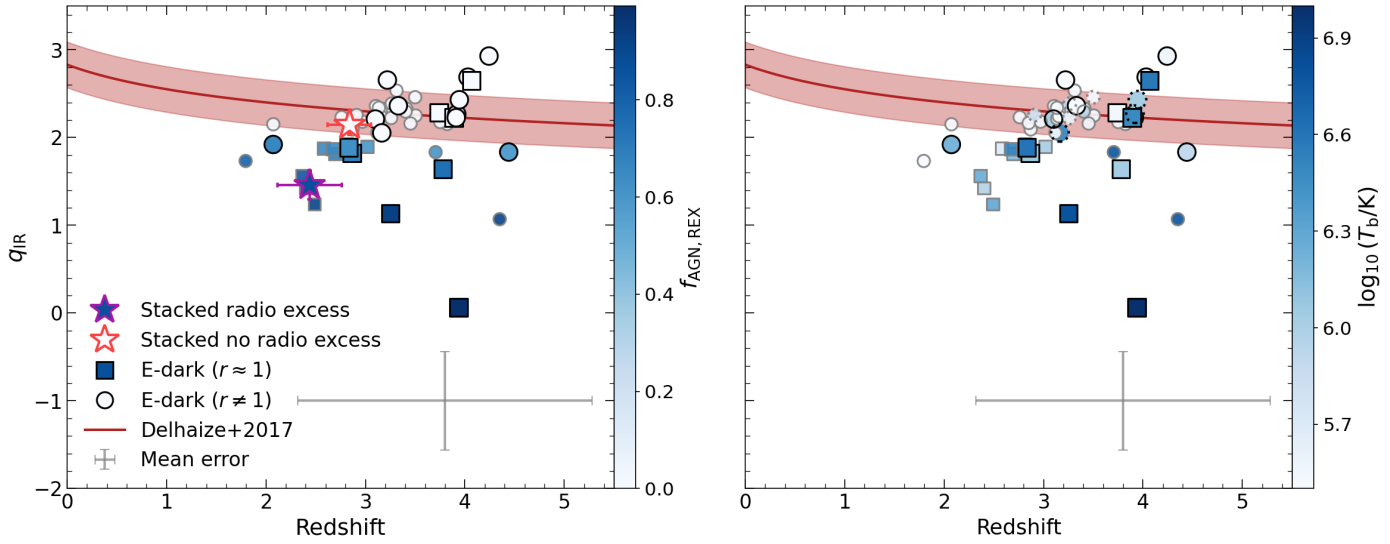


Fig. 5. *Left*: IRRC versus redshift, colour-coded according to AGN fraction values computed as described in Sect. 5. Symbols are the same as Fig. 4. Objects with at least one SPIRE detection are marked with larger symbols, while sources without SPIRE detections are shown with smaller symbols. The solid red curve represents the Delhaize et al. (2017) IRRC with its intrinsic 1σ scatter (red shaded area). The grey cross represents the mean error including all sources. The results for the stacked samples with and without radio excess, presented in Sect. 6, are shown as purple and red outlined stars, respectively. *Right*: same as the left panel but colour-coded according to the brightness temperature. Upper limits in T_b are indicated by symbols outlined with a dotted line. For clarity, we only show upper limits for sources with a detection in the LOFAR ILT high-resolution image, given that all non-detections have $\log_{10}(T_b/K) < 5.6$.

In the above expression, q is the IRRC value measured for each galaxy in our sample, while $\bar{q}(z)$ represents the value expected at the same redshift according to the relation derived by Delhaize et al. (2017). Since this relation is characterised by an intrinsic scatter of 0.26, we assigned $f_{AGN,REX} = 0$ to all sources with $q - \bar{q}(z) < 0.26$, corresponding to sources consistent within 1σ with the IRRC expected for SFGs.

Figure 5 shows the IRRC parameter for our sample as a function of the redshift and colour-coded according to AGN fraction (left panel) and T_b (right panel) values. About 34% of the sample shows an excess with respect to the IRRC, corresponding to $f_{AGN,REX} > 0.4$. A similar fraction is found among the 35 sources without LOFAR ILT coverage (see Fig. B.2), with 12 out of 35 galaxies displaying a radio excess. Focusing on the subsample of 53/88 sources with LOFAR ILT coverage, the majority of radio-excess galaxies are detected at 0.″3 at 144 MHz, with only a few exceptions discussed below. Additionally they have $r \approx 1$ and/or $\log_{10}(T_b/K) > 5.6$. Only two sources with radio excess have $\log_{10}(T_b/K) < 5.6$ and/or have no detection in the 0.″3 LOFAR image. All the remaining sources undetected in the LOFAR ILT map are located within the IRRC. A subset of galaxies (14) lying on the IRRC is detected at high angular resolution, indicating the presence of a compact radio component, despite the absence of a radio excess. Among these sources, nine objects either have an upper limit on the brightness temperature or exhibit $\log_{10}(T_b/K) < 5.6$, values that can be attributed to radio emission associated with star formation. The five remaining sources are all detected at high angular resolution and have $\log_{10}(T_b/K) > 5.6$, with two of them also characterised by $r \approx 1$. For these sources, the detection of compact radio emission with a high brightness temperature occurs despite their location on the IRRC. In Fig. 6 we show a Venn diagram illustrating the intersection between sources with $r \approx 1$, $\log_{10}(T_b/K) > 5.6$, and radio excess.

For the 26 sources with at least one FIR (SPIRE and/or SCUBA-2) detection, in Fig. 7 we report the distribution of

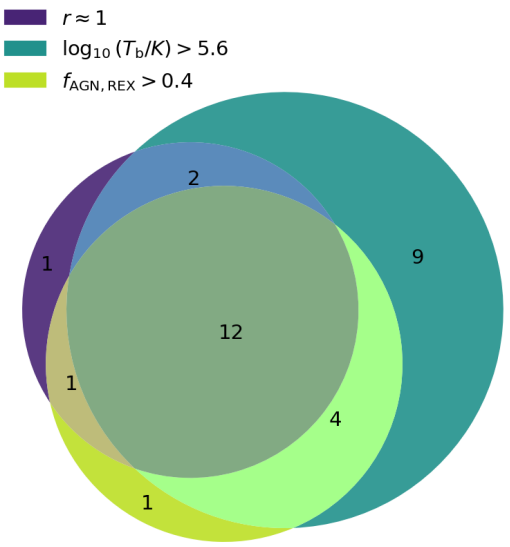


Fig. 6. Venn diagram showing the sources with overlapping criteria for identifying an AGN in the radio band: excess with respect to the IRRC, flux ratio between LOFAR high- and low-angular-resolution observations, and brightness temperature.

the dust attenuation for the ISM, the IR luminosity of the dust component integrated in the 8–1000 μm range, the SFR derived from this latter quantity using the standard calibration of Kennicutt & Evans (2012), and the stellar mass. The high obscuration values ($\langle A_V^{ISM} \rangle = 5.0$, $\sigma(A_V^{ISM}) = 0.6$) suggest high dust content, which is further supported by the inferred IR luminosity ($\langle \log_{10}(L_{IR}/L_\odot) \rangle = 13.2$, $\sigma[\log_{10}(L_{IR}/L_\odot)] = 0.3$) which and places the sample in the ultra-luminous infrared galaxies (ULIRGs) regime. This subset of FIR-detected, isolated, E-dark galaxies appears substantially more dust obscured and massive compared to the HST-to-IRAC

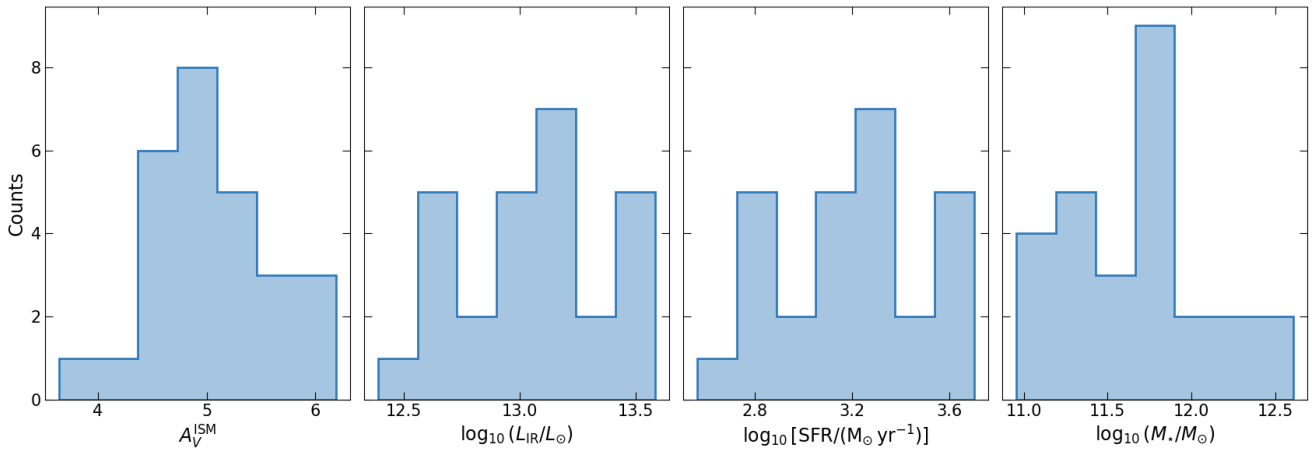


Fig. 7. Distributions of physical properties of the 26 isolated E-dark sources with at least one photometric detection in the FIR. From left to right: dust extinction of the ISM, IR luminosity, star formation rate, and stellar mass.

extremely red objects (HIERO; $H_{\rm E}$ − IRAC2 > 2.25, Wang et al. 2016) selected in the EDFs, which show a median obscuration of $A_V = 2.3$ and stellar masses of $M_\star = 4 \times 10^{10}\,M_\odot$ (Euclid Collaboration: Girardi et al. 2026). Moreover, these sources show high SFR ($\langle\log_{10}[{\rm SFR}/(M_\odot\,{\rm yr}^{-1})]\rangle = 3.3$, $\sigma(\log_{10}[{\rm SFR}/(M_\odot\,{\rm yr}^{-1})]) = 0.2$) and stellar masses ($\langle\log M_\star/(M_\odot)\rangle = 11.6$, $\sigma[\log(M_\star/M_\odot)] = 0.4$).

In Fig. 8 we show the main sequence (MS; Rodighiero et al. 2010; Euclid Collaboration: Enia et al. 2026) of SFGs of Popesso et al. (2023). We compare our results with samples obtained in the literature for similar selections (Talia et al. 2021; G24; G25), as well as with sub-millimetre galaxy samples such as the AS2UDS galaxies (Stach et al. 2019; Dudzevičiūtė et al. 2020) selected to be undetected at $K \gtrsim 25.7$.

We focus our discussion on the $2.6 \leq z < 3.6$ redshift bin, which includes the bulk of the sources (see Fig. 3). We also included the MS relation by Popesso et al. (2023) computed at the mean redshift of $z = 3$. The estimated median for the SFR and stellar mass locates the FIR-detected, isolated, E-dark galaxies at approximately 0.7 dex above the MS at $z = 3$. This subset of 26 galaxies is therefore compatible with starburst systems, spanning stellar mass ranges similar to those of the RS–NIR dark/faint galaxies presented in Talia et al. (2021), while overlapping with the high-mass end of the RS–NIR dark samples of G24 and G25, as well as with the high-mass range of sub-millimetre–selected galaxies (Dudzevičiūtė et al. 2020). Similarly, our sources tend to populate the upper end of the distribution of star formation rate with respect to these samples. By comparing the median SFR of the various samples, we find a $\Delta\log_{10}[{\rm SFR}/(M_\odot\,{\rm yr}^{-1})] \approx 0.3$ dex relative to G24 and Talia et al. (2021) and a $\Delta\log_{10}[{\rm SFR}/(M_\odot\,{\rm yr}^{-1})] \approx 0.5$ dex when compared to G25 and Dudzevičiūtė et al. (2020). This behaviour can be explained by the fact that our subset is detected in shallower FIR observations than those adopted in these works (e.g. Oliver et al. 2012), favouring intrinsically brighter and more actively star-forming systems. As a consequence, our FIR-detected galaxies represent the more extreme end of the distributions already traced by similar high-redshift samples.

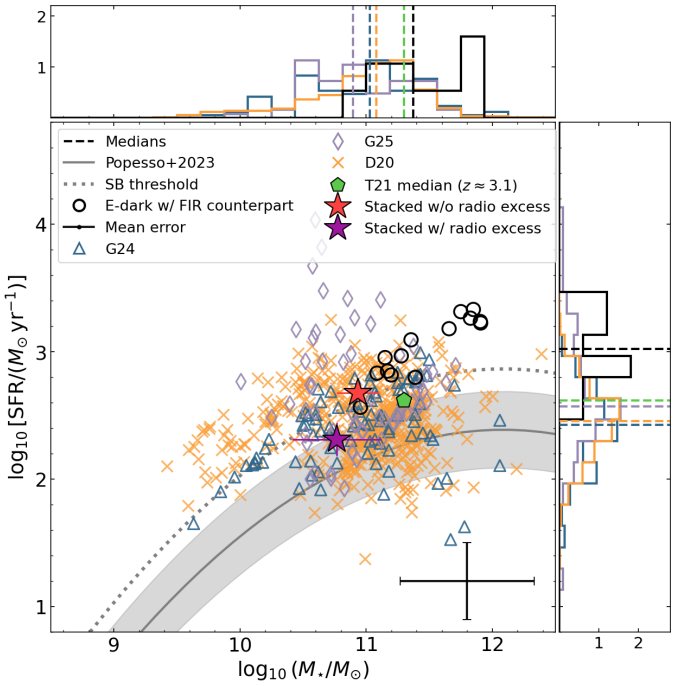


Fig. 8. Star formation rate versus stellar mass for the redshift bin $2.6 \leq z \leq 3.6$. Empty black circles show our sample of isolated E-dark sources with at least one FIR detection. The black cross reports the mean uncertainty. Our results are compared with the MS from Popesso et al. (2023, at $z = 3$). The dotted line represents the threshold for considering a galaxy as a starburst (i.e. 3× the SFR of MS galaxies from Popesso et al. 2023). RS-NIR dark or faint galaxies are shown as blue triangles (G24) and purple diamonds (G25). For the RS-NIR dark galaxies of Talia et al. (2021), we report the median value of the sample as a green pentagon. We also show the sample of sub-millimetre galaxies from Dudzevičiūtė et al. (2020, orange crosses). Purple and red stars represent the results for the stacked samples of our objects with and without radio excess, respectively (see Sect. 6). The top and right panels show the distributions for the stellar mass and SFR for each sample, and the dashed lines represent the respective median values.

6. Stacking

To further validate and complement the results obtained for the individual sources, we performed a median stacking analysis including all 53 objects, divided according to the presence or absence of a radio excess, as identified in Sect. 5. These two samples consist of 18 and 35 objects, respectively. This approach

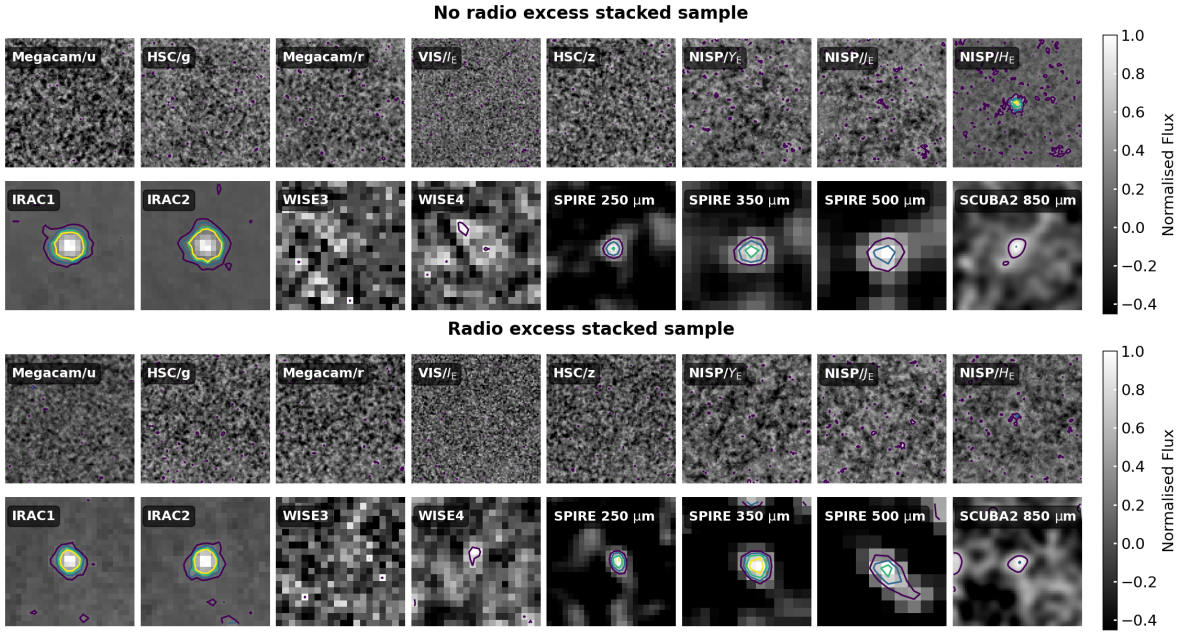


Fig. 9. Images of median-stacked samples across wavebands from the UV to the FIR. The top and bottom sets of 12 images refer to our two stacked samples, respectively, without and with radio excess. Each cutout is normalised to its peak pixel value. Contours display the 3, 5, 7, and 9σ emission. Postage stamps are $10'' \times 10''$ for Megacam, HSC, and *Euclid*; $15'' \times 15''$ for IRAC; $50'' \times 50''$ for WISE; and $150'' \times 150''$ for SPIRE and SCUBA-2.

enabled us to extract statistical information on the average properties of both subsets. We stacked the available optical-to-FIR and low-resolution radio-image cutouts, centred at the IRAC2 positions of our targets. For WISE, we adopted the unblurred unWISE images. Following Euclid Collaboration: Hill et al. (2026), we performed stacking using the non-matched-filtered SPIRE and SCUBA-2 maps. SCUBA-2 covers, respectively, ten and nine sources among the non-radio-excess and radio-excess samples. The resulting median stacked optical-to-FIR images are shown in Fig. 9.

We built the median SED by extracting the photometry in each available filter as follows. Flux densities were derived using the aperture photometry function of `PHOTUTILS`, assuming a circular aperture centred at the IRAC position. The diameter of the circular aperture was selected in relation to the flattening of the radial brightness profile of the source and corresponds to 1″ for *Euclid*, 6″ for IRAC, and 9″ for LOFAR. Both samples are undetected up to the NISP J_E band and become detectable at a significance of $\approx 9\sigma$ and $\approx 3\sigma$ in H_E for the non-radio-excess and radio-excess samples, respectively.

We repeated the SED fitting with the same configuration described in Sect. 4.3. Although the SCUBA-2 stacking does not cover the full extent of both samples, we assume that the objects, which are randomly distributed across the map, are representative of the overall populations. To verify that the SED fitting is not biased by the subset of sources within the SCUBA-2 coverage, we also repeated the analysis excluding these points as a consistency check. In Table 4 and Fig. 10, we report the physical properties and the best-fit SED for the median stacked photometry in terms of output from `CIGALE` for the two samples with and without radio excess[5].

[5] Excluding the SCUBA-2 points from the SED fitting does not produce significant differences in the results, although the uncertainties on the derived parameters are higher. For example, we obtain $z_{ph} = 3.0 \pm 0.6$, $\chi^2_{red} = 0.3$ and $z_{ph} = 2.7 \pm 0.7$, $\chi^2_{red} = 0.2$ for the samples without and with radio excess, respectively.

The two samples exhibit comparable dust attenuation and show modest differences in redshift, stellar mass, and SFR, with the radio-excess sources having somewhat lower values on average. The stacked sample of non-radio-excess sources lies within the intrinsic scatter of the IRRC at the corresponding redshift ($z_{ph} = 2.8 \pm 0.2$), corresponding to an AGN fraction of $f_{AGN,REX} = 0.3 \pm 0.2$, with a q_{IR} value lower than the expected value for SFGs by 0.17 dex predicted by Delhaize et al. (2017). The radio-excess stacked sample shows a well-constrained radio excess, with an AGN fraction of $f_{AGN,REX} = 0.87 \pm 0.05$. For both stacked samples, the radio-loudness parameter, R_{AGN}, is poorly constrained, with `CIGALE` returning best-fit values of $R_{AGN} = 0$ and $R_{AGN} = 1000$ for the non-radio-excess and radio-excess stacked samples, respectively, where $R_{AGN} = 10$ is commonly adopted as the boundary between radio-quiet and radio-loud AGNs (Kellermann et al. 1989).

Both stacked samples are found to lie above the locus of the star-forming MS at their corresponding photometric redshift of $z_{ph} = 2.8$ and $z_{ph} = 2.4$ for the samples without and with radio excess, respectively. The non-radio-excess stacked sample shows an offset of ≈ 0.6 dex with respect to the MS, while the radio-excess stacked sample is offset by approximately 0.4 dex. Given the typical intrinsic scatter of the main sequence of 0.3 dex, the former sample can be classified as a starburst population, while the latter lies below the threshold to consider a galaxy as a starburst. At the same time, their high SFR suggests that they are not strictly representative of the bulk of main-sequence galaxies.

7. Discussion

In this paper, we present the first sample of E-dark galaxies selected in the radio band within the EDF-N field. Unlike previous studies, which mainly relied on 1.4 GHz and 3 GHz observations, our selection is based on deep, low-frequency (144 MHz) LOFAR HBA data, reaching an RMS sensitivity limit of 32 μJy beam^{-1}. Moreover, the EDF-N spans an area at least

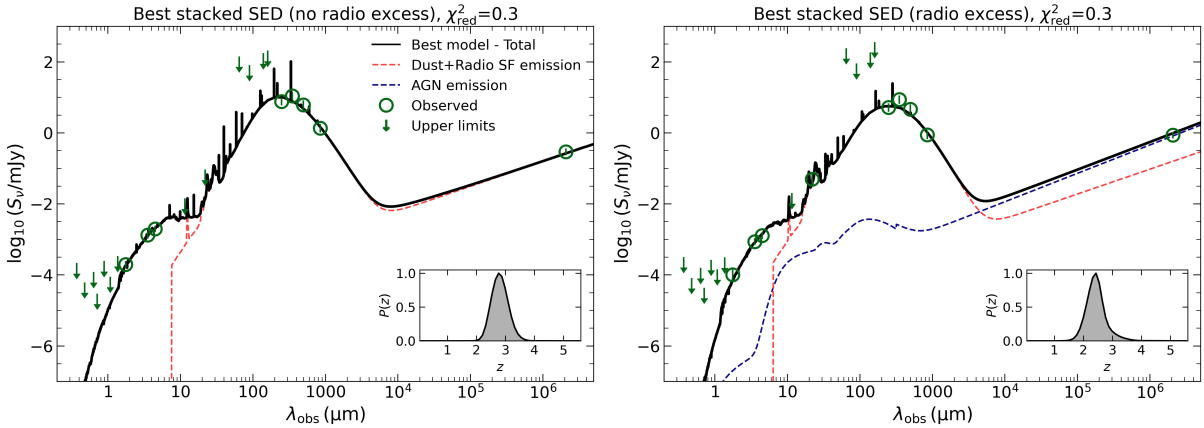


Fig. 10. Best-fit SEDs from CIGALE for the median stacked photometry of the two samples with and without radio-excess. Empty green circles mark the photometric detections and arrows the 3σ upper limits. The solid black line shows the total modelled emission. The dashed blue line represents the AGN contribution, including the radio component, while the dashed red line corresponds to the dust and radio emission from the host galaxy. The insert shows the probability distribution of the photometric redshift. Reported wavelengths are in the observed frame.

Table 4. Output parameters from CIGALE and derived quantities.

SED-fitting results for stacking		
	No REX	REX
z_{ph}	2.8 ± 0.2	2.4 ± 0.3
$\log_{10}(M_\star/M_\odot)$	10.9 ± 0.2	10.7 ± 0.4
$A_{V,\mathrm{ISM}}$	4.5 ± 0.2	5.1 ± 0.9
$\log_{10}[L_{1.4\,\mathrm{GHz,AGN}}/(\mathrm{W\,Hz^{-1}})]$	[0]	24.8 ± 0.2
R_{AGN}	[0]	[1000]
$\log_{10}(t/\mathrm{Myr})$	2.8 ± 0.1	2.9 ± 0.1
$\log_{10}(\tau/\mathrm{Myr})$	[3.0]	[2.7]
α_{d}	1.01 ± 0.08	1.4 ± 0.2
Ψ/deg	$[1 \times 10^{-3}]$	$[1 \times 10^{-3}]$
$\log_{10}(L_{\mathrm{IR}}/L_\odot)$	12.6 ± 0.1	12.2 ± 0.1
$\log_{10}[L_{1.4\,\mathrm{GHz,SF}}/(\mathrm{W\,Hz^{-1}})]$	24.42 ± 0.01	23.2 ± 0.1
$\log_{10}[\mathrm{SFR_{IR}}/(M_\odot\ \mathrm{yr^{-1}})]$	2.7 ± 0.1	2.3 ± 0.1
q_{IR}	2.1 ± 0.1	1.2 ± 0.2
$f_{\mathrm{AGN,REX}}$	0.3 ± 0.2	0.89 ± 0.06

Notes. Results are shown for the two stacked samples (i.e. sources with and without radio excess). From the first row: photometric redshift, stellar mass, V-band attenuation for the ISM, AGN radio luminosity at 1.4 GHz, radio loudness parameter, stellar age, e-folding time of the main stellar population, dust slope, and AGN viewing angle. The last five rows report the parameters computed from the SED-fitting outputs: the IR luminosity of the galaxy computed in the 8–1000 μm range; the 1.4 GHz luminosity from star formation processes, derived by subtracting the AGN contribution to the total radio luminosity at 1.4 GHz and computed assuming a simple power-law spectrum $S_\nu \propto \nu^\alpha$ with $\alpha = -0.7$; the SFR inferred from the infrared luminosity exploiting the calibration of Kennicutt & Evans (2012); the IR/radio correlation parameter; and the AGN fraction computed following G25. For parameters whose Bayesian estimate is not constrained from the fit (i.e. the uncertainty is higher than the parameter value), we report the best-fit value from the input grid provided by CIGALE in square brackets.

five times larger than previous studies, which were typically limited to smaller fields such as COSMOS and GOODS-N.

A first key difference lies in the low surface density of E-dark sources when compared to similar selections. Our selection yielded 166 E-dark galaxies across approximately 10 deg^2, corresponding to a surface density of approximately 17 sources per square degree. For comparison, Enia et al. (2022) found a surface density of ≈ 360 sources per deg^2, while the RS-NIR dark galaxies found in G24 and G25 have a surface density of approximately 190 and 235 sources per deg^2, respectively.

The number of sources retrieved in this paper is therefore relatively small when compared to previous samples of RS-NIR dark objects, considering that the observations exploited cover a larger area; however, a direct quantitative comparison between the samples and their number densities is hindered by the varying depths, angular resolutions, and selection criteria adopted across these studies. We therefore focused on the main differences between our selection and those adopted in previous studies. First, given that our methodology uses the B25 catalogue as a starting point, our parent sample is, by construction, limited to sources with counterparts in *Spitzer*/IRAC1 and IRAC2, whose observations in the EDF-N are about one order of magnitude shallower than those conducted in COSMOS. Secondly, our selection criteria might be more stringent during the visual inspection step because we relied on lower resolution LOFAR (1.″5) and IRAC (≈2″) data. At this resolution, multiple sources or contaminants may fall within the radio and infrared emissions, increasing the number of objects rejected during visual inspection compared to studies based on higher resolution data (e.g. JVLA in COSMOS). Moreover, when comparing the different radio observations, the sensitivity of LOFAR observations used in this work would reach approximately 3.8 μJy beam^{-1} at 3 GHz (assuming a radio spectral index of −0.7), which is about a factor 1.5 higher when compared to the VLA-COSMOS 3 GHz Large Project survey (1σ = 2.3 μJy beam^{-1}) exploited in Talia et al. (2021), G24, and G25 (see Fig. 11). The relatively shallower radio sensitivity implies that our sample is limited to fewer, brighter sources, thereby excluding the fainter dark galaxies, which, as shown in Fig. 11, make up the bulk of the distribution in the sample of Rs–NIR dark sources from G24.

We analysed a sample of 88 isolated E-dark galaxies, focusing on 53 sources covered by high-resolution LOFAR ILT observations at 0.″3 over an area of approximately 2.5 deg × 2.5 deg. The compact radio emission, particularly the ratio between high- and low-resolution fluxes, provided constraints on its origin and on the potential presence of AGN activity. By performing SED fitting using the CIGALE code, we were able to estimate the brightness temperatures T_{b} (or upper limits) and combine

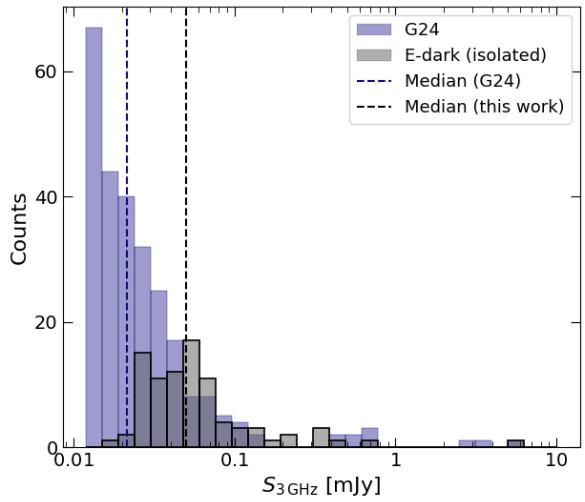


Fig. 11. Comparison between distributions of flux density at 3 GHz of our sample of isolated E-dark sources (grey histogram) and the RS-NIR dark galaxies of G24 (blue histogram). The dashed vertical lines represent the median values of the distributions.

this information with the placement of these sources on the IRRC.

Our analysis shows that roughly one-third of the sample exhibits a radio excess relative to the IRRC, corresponding to an AGN fraction of $f_{\mathrm{AGN,REX}} > 0.4$. This fraction increases to 40% when including AGNs identified via brightness temperature. In general, the radio excess in our galaxies is associated with brightness temperatures exceeding the threshold typically used to classify objects as starbursts, whereas sources consistent with the IRRC are largely compatible with radio emission driven by star formation, with some exceptions. These exceptions likely correspond to cases with more uncertain classifications, where the radio emission is confined to sub-kiloparsec scales and could be associated with radio-quiet AGNs (e.g. Morabito et al. 2022). A lower abundance of radio-excess systems has been reported in similar selections based on smaller area surveys. For instance, G24 found that ∼20% of their Rs–NIR dark sample shows evidence of AGN activity when combining multiple diagnostics, such as X-ray emission and SED decomposition, while only ∼14% display a radio excess when considering only the distance from the IRRC as a criterion. The higher number of radio-excess sources in our sample can be naturally explained by the wider area and relatively shallower radio coverage provided by LOFAR, which biases our selection towards the brighter end of the radio-bright and obscured population.

For 26 objects with FIR counterparts, we were able to derive estimates of the SFR and other physical properties with higher reliability. These sources represent the more extreme end of the distribution, corresponding to massive ($M_\star \approx 10^{11}\,M_\odot$), obscured ($A_V^{\mathrm{ISM}} \approx 5$), highly star-forming (SFR $\approx 4 \times 10^3\,M_\odot\,\mathrm{yr}^{-1}$) galaxies at intermediate redshift ($z \approx 3$), occupying the starburst locus in the SFR versus stellar mass diagram.

We performed a stacking analysis, dividing our sources into two samples according to their radio excess with respect to the IRRC. The results from the SED fitting point out that the two samples display similar global physical properties, while differing primarily in their radio emission. The physical properties are consistent with the trends observed for individual sources, but less extreme in terms of SFR. This is expected, as these stacked sources are fainter in the FIR. Nonetheless, they generally occupy the transition region between the main sequence and starburst populations at $z = 3$. The non-radio-excess stacked sample is consistent with SFGs lying within the IRRC scatter, with no significant indications of AGN-related radio emission. In contrast, the radio-excess sample shows a clear and well-constrained radio excess, which is consistent with a dominant AGN contribution. Interestingly, these results highlight that our selection efficiently identifies not only heavily obscured SFGs, but also obscured AGNs at high redshift, with a significant fraction of sources exhibiting a radio excess and/or high T_b values while still hosting significant ongoing star formation. In contrast to previous selections based on smaller area surveys, which predominantly targeted SFGs, the wider area coverage explored in this work reveals a more heterogeneous population of obscured systems, where intense star formation and significant AGN activity coexist.

Our work, therefore, highlights the power wide-field surveys have, such as those enabled by *Euclid*, to uncover rare and heavily obscured populations. In this broader context, our analysis is a valuable pilot study to guide future selections of such populations, which offer a unique opportunity to investigate the co-evolution of galaxies and AGNs (e.g. Mancuso et al. 2017; Lapi et al. 2018).

Nonetheless, this interpretation requires further confirmation through more robust analysis, as the current limitations in photometric coverage affect the reliability of the physical properties derived via SED fitting. Future *Euclid* data releases, offering deeper observations, will also improve the characterisation of these sources and allow a more accurate determination of their contribution to the cosmic SFRD. The *Euclid* Data Release 1 observations are expected to include a total of 11 visits in the EDF-N, providing an additional gain in sensitivity of approximately 1.3 mag with respect to Q1. Moreover, the JWST offers the possibility to follow up on these galaxies through MIRI imaging, providing direct constraints on MIR emission and enabling a more reliable separation between star formation and AGN contributions in radio-selected E-dark galaxies.

Data availability

The table listing the 88 isolated E-dark galaxies and their physical properties is available at the CDS via https://cdsarc.cds.unistra.fr/viz-bin/cat/J/A+A/714/A210.

Acknowledgements. M.G. and I.P. acknowledge support from INAF under the following funding schemes: Large Grant 2022 (project "MeerKAT and LOFAR Team up: a Unique Radio Window on Galaxy/AGN co-Evolution") and Large GO 2024 (project "MeerKAT and Euclid Team up: Exploring the galaxy-halo connection at cosmic noon"). A.L.M. acknowledges support through the European Space Agency (ESA) Research Fellowship in Space Science. We thank Smail I. for the helpful comments. The Euclid Consortium acknowledges the European Space Agency and a number of agencies and institutes that have supported the development of *Euclid*, in particular the Agenzia Spaziale Italiana, the Austrian Forschungsförderungsgesellschaft funded through BMK, the Belgian Science Policy, the Canadian Euclid Consortium, the Deutsches Zentrum für Luft- und Raumfahrt, the DTU Space and the Niels Bohr Institute in Denmark, the French Centre National d'Etudes Spatiales, the Fundação para a Ciência e a Tecnologia, the Hungarian Academy of Sciences, the Ministerio de Ciencia, Innovación y Universidades, the National Aeronautics and Space Administration, the National Astronomical Observatory of Japan, the Netherlandse Onderzoekschool Voor Astronomie, the Norwegian Space Agency, the Research Council of Finland, the Romanian Space Agency, the State Secretariat for Education, Research, and Innovation (SERI) at the Swiss Space Office (SSO), and the United Kingdom Space Agency. A complete and detailed list is available on the *Euclid* web site (www.euclid-ec.org). A complete list of acknowledgements is available on https://www.euclid-ec.org/consortium/community/. This work has made use of the *Euclid* Quick Release Q1 data from the *Euclid* mission of the European Space Agency (ESA),

2025, https://doi.org/10.57780/esa-2853f3b. This research makes use of ESA Datalabs (datalabs.esa.int), an initiative by ESA's Data Science and Archives Division in the Science and Operations Department, Directorate of Science. Based on data from UNIONS, a scientific collaboration using three Hawaii-based telescopes: CFHT, Pan-STARRS, Subaru www.skysurvey.cc. This publication is based on observations made with the Spitzer Space Telescope, which is operated by the Jet Propulsion Laboratory, California Institute of Technology, under a contract with NASA, and has made use of the NASA/IPAC Infrared Science Archive, which is funded by the National Aeronautics and Space Administration and operated by the California Institute of Technology. This publication makes use of the mosaics from the Spitzer Enhanced Imaging Products (SEIP, https://doi.org/10.26131/IRSA433). The Wide-field Infrared Survey Explorer is a joint project of the University of California, Los Angeles, and the Jet Propulsion Laboratory/California Institute of Technology, funded by the National Aeronautics and Space Administration. This paper is based on observations with AKARI, a JAXA project with the participation of ESA. Herschel is an ESA space observatory with science instruments provided by European-led Principal Investigator consortia and with important participation from NASA. This work is based on data from the SPIRE Point Source Catalogue (https://doi.org/10.5270/esa-6gfkpzh). The Herschel Extragalactic Legacy Project, (HELP), is a European Commission Research Executive Agency funded project under the SP1-Cooperation, Collaborative project, Small or medium-scale focused research project, FP7-SPACE-2013-1 scheme, Grant Agreement Number 607254. This research made use of Photutils, an Astropy package for detection and photometry of astronomical sources (Bradley et al. 2023).

References

Barrufet, L., Oesch, P. A., Weibel, A., et al. 2023, MNRAS, 522, 449
Behiri, M., Talia, M., Cimatti, A., et al. 2023, ApJ, 957, 63
Bell, E. F. 2003, ApJ, 586, 794
Bisigello, L., Giulietti, M., Prandoni, I., et al. 2025, Open J. Astrophys., 8, 101
Bonato, M., Negrello, M., Mancuso, C., et al. 2017, MNRAS, 469, 1912
Bondi, M., Scaramella, R., Zamorani, G., et al. 2024, A&A, 683, A179
Boquien, M., Burgarella, D., Roehlly, Y., et al. 2019, A&A, 622, A103
Bradley, L., Sipőcz, B., Robitaille, T., et al. 2023, https://doi.org/10.5281/zenodo.1035865
Bruzual, G., & Charlot, S. 2003, MNRAS, 344, 1000
Ceraj, L., Smolčić, V., Delvecchio, I., et al. 2018, A&A, 620, A192
Chabrier, G. 2003, PASP, 115, 763
Chapman, S. C., Richards, E. A., Lewis, G. F., Wilson, G., & Barger, A. J. 2001, ApJ, 548, L147
Chapman, S. C., Smail, I., Blain, A. W., & Ivison, R. J. 2004, ApJ, 614, 671
Charlot, S., & Fall, S. M. 2000, ApJ, 539, 718
Condon, J. J., Huang, Z.-P., Yin, Q. F., & Thuan, T. X. 1991, ApJ, 378, 65
Condon, J. J., Cotton, W. D., & Broderick, J. J. 2002, AJ, 124, 675
Dale, D. A., Helou, G., Magdis, G. E., et al. 2014, ApJ, 784, 83
de Ruiter, H. R., Willis, A. G., & Arp, H. C. 1977, A&AS, 28, 211
Delhaize, J., Smolčić, V., Delvecchio, I., et al. 2017, A&A, 602, A4
Dickinson, M., Papovich, C., Ferguson, H. C., & Budavári, T. 2003, ApJ, 587, 25
Doi, Y., Takita, S., Ootsubo, T., et al. 2015, PASJ, 67, 50
Dudzevičiūtė, U., Smail, I., Swinbank, A. M., et al. 2020, MNRAS, 494, 3828
Enia, A., Talia, M., Pozzi, F., et al. 2022, ApJ, 927, 204
Euclid Collaboration (Moneti, A., et al.) 2022, A&A, 658, A126
Euclid Collaboration (Cropper, M., et al.) 2025, A&A, 697, A2
Euclid Collaboration (Jahnke, K., et al.) 2025, A&A, 697, A3
Euclid Collaboration (McPartland, C. J. R., et al.) 2025, A&A, 695, A259
Euclid Collaboration (Mellier, Y., et al.) 2025, A&A, 697, A1
Euclid Collaboration (Aussel, H., et al.) 2026, A&A, 711, A1
Euclid Collaboration (Enia, A., et al.) 2026, A&A, 711, A14
Euclid Collaboration (Girardi, G., et al.) 2026, A&A, 711, A22
Euclid Collaboration (Hill, R., et al.) 2026, A&A, 711, A23
Euclid Collaboration (McCracken, H. J., et al.) 2026, A&A, 711, A2
Euclid Collaboration Polenta, G., et al.) 2026, A&A, 711, A3
Euclid Collaboration (Romelli, E., et al.) 2026, A&A, 711, A4
Euclid Quick Release Q1 2025, https://doi.org/10.57780/esa-2853f3b
Franco, M., Elbaz, D., Béthermin, M., et al. 2018, A&A, 620, A152
Fritz, J., Franceschini, A., & Hatziminaoglou, E. 2006, MNRAS, 366, 767
Fudamoto, Y., Oesch, P. A., Schouws, S., et al. 2021, Nature, 597, 489
Gentile, F., Talia, M., Behiri, M., et al. 2024, ApJ, 962, 26
Gentile, F., Talia, M., Enia, A., et al. 2025, A&A, 697, A46
Giavalisco, M., Ferguson, H. C., Koekemoer, A. M., et al. 2004, ApJ, 600, L93
Gruppioni, C., Béthermin, M., Loiacono, F., et al. 2020, A&A, 643, A8
Gwyn, S., McConnachie, A. W., Cuillandre, J.-C., et al. 2025, AJ 170, 324
Helou, G., Soifer, B. T., & Rowan-Robinson, M. 1985, ApJ, 298, L7
Hickox, R. C., & Alexander, D. M. 2018, ARA&A, 56, 625
Hopkins, P. F., Hernquist, L., Cox, T. J., & Kereš, D. 2008, ApJS, 175, 356
Hurley, P. 2017, XID+: Next generation XID development, Astrophysics Source Code Library [record ascl:1704.012]
Inoue, A. K. 2011, MNRAS, 415, 2920
Ivison, R. J., Alexander, D. M., Biggs, A. D., et al. 2010a, MNRAS, 402, 245
Ivison, R. J., Magnelli, B., Ibar, E., et al. 2010b, A&A, 518, L31
Jarrett, T. H., Cohen, M., Masci, F., et al. 2011, ApJ, 735, 112
Kawada, M., Baba, H., Barthel, P. D., et al. 2007, PASJ, 59, S389
Kellermann, K. I., Sramek, R., Schmidt, M., Shaffer, D. B., & Green, R. 1989, AJ, 98, 1195
Kennicutt, R. C., & Evans, N. J. 2012, ARA&A, 50, 531
Lang, D. 2014, AJ, 147, 108
Lapi, A., Pantoni, L., Zanisi, L., et al. 2018, ApJ, 857, 22
Mainzer, A., Grav, T., Bauer, J., et al. 2011, ApJ, 743, 156
Mancuso, C., Lapi, A., Prandoni, I., et al. 2017, ApJ, 842, 95
Manning, S. M., Casey, C. M., Zavala, J. A., et al. 2022, ApJ, 925, 23
Marton, G., Calzoletti, L., Perez Garcia, A. M., et al. 2017, arXiv e-prints [arXiv:1705.05693]
Mazzolari, G., Gilli, R., Brusa, M., et al. 2024, A&A, 687, A120
Morabito, L. K., Sweijen, F., Radcliffe, J. F., et al. 2022, MNRAS, 515, 5758
Morabito, L. K., Jackson, N., de Jong, J., et al. 2025a, Ap&SS, 370, 19
Morabito, L. K., Kondapally, R., Best, P. N., et al. 2025b, MNRAS, 536, L32
Novak, M., Smolčić, V., Delhaize, J., et al. 2017, A&A, 602, A5
Oke, J. B., & Gunn, J. E. 1983, ApJ, 266, 713
Oliver, S. J., Bock, J., Altieri, B., et al. 2012, MNRAS, 424, 1614
Owen, F. N. 2018, ApJS, 235, 34
Panessa, F., Baldi, R. D., Laor, A., et al. 2019, Nat. Astron., 3, 387
Pearson, C., Cheale, R., Serjeant, S., et al. 2017a, Publ. Korean Astron. Soc., 32, 219
Pearson, W. J., Wang, L., van der Tak, F. F. S., et al. 2017b, A&A, 603, A102
Pearson, W. J., Wang, L., Hurley, P. D., et al. 2018, A&A, 615, A146
Popesso, P., Concas, A., Cresci, G., et al. 2023, MNRAS, 519, 1526
Prandoni, I., Guglielmino, G., Morganti, R., et al. 2018, MNRAS, 481, 4548
Riechers, D. A., Boogaard, L. A., Decarli, R., et al. 2020, ApJ, 896, L21
Rodighiero, G., Vaccari, M., Franceschini, A., et al. 2010, A&A, 515, A8
Sargent, M. T., Schinnerer, E., Murphy, E., et al. 2010, ApJ, 714, L190
Schober, J., Schleicher, D. R. G., & Klessen, R. S. 2017, MNRAS, 468, 946
Schreiber, C., Glazebrook, K., Nanayakkara, T., et al. 2018, A&A, 618, A85
Schulz, B., Marton, G., Valtchanov, I., et al. 2018, in American Astronomical Society Meeting Abstracts, 231, 361.21
Scoville, N., Aussel, H., Brusa, M., et al. 2007, ApJS, 172, 1
Shim, H., Kim, Y., Lee, D., et al. 2020, MNRAS, 498, 5065
Shirley, R., Roehlly, Y., Hurley, P. D., et al. 2019, MNRAS, 490, 634
Shirley, R., Duncan, K., Campos Varillas, M. C., et al. 2021, MNRAS, 507, 129
Shu, X., Yang, L., Liu, D., et al. 2022, ApJ, 926, 155
Simpson, J. M., Swinbank, A. M., Smail, I., et al. 2014, ApJ, 788, 125
Smail, I., Owen, F. N., Morrison, G. E., et al. 2002, ApJ, 581, 844
Smail, I., Dudzevičiūtė, U., Stach, S. M., et al. 2021, MNRAS, 502, 3426
Smolčić, V., Novak, M., Delvecchio, I., et al. 2017, A&A, 602, A6
Stach, S. M., Dudzevičiūtė, U., Smail, I., et al. 2019, MNRAS, 487, 4648
Sun, F., Egami, E., Pérez-González, P. G., et al. 2021, ApJ, 922, 114
Sutherland, W., & Saunders, W. 1992, MNRAS, 259, 413
Talia, M., Cimatti, A., Giulietti, M., et al. 2021, ApJ, 909, 23
Taylor, A. J., Barger, A. J., Cowie, L. L., et al. 2023, ApJS, 266, 24
Valentino, F., Tanaka, M., Davidzon, I., et al. 2020, ApJ, 889, 93
van der Vlugt, D., Algera, H. S. B., Hodge, J. A., et al. 2021, ApJ, 907, 5
van der Vlugt, D., Hodge, J. A., Algera, H. S. B., et al. 2022, ApJ, 941, 10
van der Vlugt, D., Hodge, J. A., Jin, S., et al. 2023, ApJ, 951, 131
Wang, F., Wu, X.-B., Fan, X., et al. 2016, ApJ, 819, 24
Wang, T., Schreiber, C., Elbaz, D., et al. 2019, Nature, 572, 211
Williams, C. C., Labbe, I., Spilker, J., et al. 2019a, ApJ, 884, 154
Williams, W. L., Hardcastle, M. J., Best, P. N., et al. 2019b, A&A, 622, A2
Wang, L., Gao, F., Best, P. N., et al. 2021, A&A, 648, A8
Wright, E. L., Eisenhardt, P. R. M., Mainzer, A. K., et al. 2010, AJ, 140, 1868
Xiao, M. Y., Elbaz, D., Gómez-Guijarro, C., et al. 2023, A&A, 672, A18
Xiao, M., Oesch, P. A., Elbaz, D., et al. 2024, Nature, 635, 311
Yamamura, I., Makiuti, S., Ikeda, N., et al. 2009, in Exoplanets and Disks: Their Formation and Diversity, eds. T. Usuda, M. Tamura, & M. Ishii (AIP), American Institute of Physics Conference Series, 1158, 169
Yang, G., Boquien, M., Brandt, W. N., et al. 2022, ApJ, 927, 192
Yun, M. S., Reddy, N. A., & Condon, J. J. 2001, ApJ, 554, 803

Authors and affiliations

Euclid Collaboration: M. Giulietti[1,⋆], I. Prandoni[1], L. Bisigello[2], G. Rodighiero[3,2], M. Talia[4,5], F. Gentile[6,5], G. Girardi[3,2], M. Bondi[1], L. Wang[7,8], A. La Marca[9], P. A. C. Cunha[10], R. Hill[11], A. Abghari[11], D. Scott[11], G. Zamorani[5], G. A. Mamon[12,13], A. Lapi[14,15,1,16], M. Behiri[5], G. Santhosh[1,4], H. J. A. Rottgering[17], R. Gilli[5], R. Scaramella[18], G. Gandolfi[18], S. Andreon[19], N. Auricchio[5], C. Baccigalupi[15,20,16,14], M. Baldi[10,5,21], A. Balestra[2], S. Bardelli[5], P. Battaglia[5], A. Biviano[20,15], M. Bolzonella[5], E. Branchini[22,23,19], M. Brescia[24,25], J. Brinchmann[26,27,28], S. Camera[29,30,31], G. Cañas-Herrera[9,17], V. Capobianco[31], C. Carbone[32], J. Carretero[33,34], S. Casas[35,36], M. Castellano[18], G. Castignani[5], S. Cavuoti[25,37], K. C. Chambers[38], A. Cimatti[39], C. Colodro-Conde[40], G. Congedo[41], C. J. Conselice[42], L. Conversi[43,44], Y. Copin[45], A. Costille[46], F. Courbin[47,48,49], H. M. Courtois[50], M. Cropper[51], A. Da Silva[52,53], H. Degaudenzi[54], G. De Lucia[20], C. Dolding[51], H. Dole[55], F. Dubath[54], C. A. J. Duncan[41], X. Dupac[44], S. Dusini[56], S. Escoffier[57], M. Farina[58], R. Farinelli[5], F. Faustini[18,59], S. Ferriol[45], F. Finelli[5,60], S. Fotopoulou[61], M. Frailis[20], E. Franceschi[5], M. Fumana[32], L. Gabarra[62], S. Galeotta[20], K. George[63], B. Gillis[41], C. Giocoli[5,21], J. Gracia-Carpio[64], A. Grazian[2], F. Grupp[64,65], S. Gwyn[66], W. G. Hartley[54], S. V. H. Haugan[67], S. Hemmati[68], J. Hoar[44], W. Holmes[69], A. Hornstrup[70,71], M. Huertas-Company[40,72,73,74], K. Jahnke[75], M. Jhabvala[76], B. Joachimi[77], E. Keihänen[78], S. Kermiche[57], A. Kiessling[69], M. Kilbinger[79], B. Kubik[45], M. Kümmel[65], M. Kunz[80], H. Kurki-Suonio[81,82], A. M. C. Le Brun[83], S. Ligori[31], P. B. Lilje[67], V. Lindholm[81,82], I. Lloro[84], M. Magliocchetti[58], G. Mainetti[85], D. Maino[86,32,87], E. Maiorano[5], O. Mansutti[20], S. Marcin[88], O. Marggraf[89], M. Martinelli[18,90], N. Martinet[46], F. Marulli[4,5,21], R. J. Massey[91], N. Mauri[39,21], E. Medinaceli[5], S. Mei[92,93], Y. Mellier[13,12,⋆⋆†], M. Meneghetti[5,21], E. Merlin[18], G. Meylan[94], P. Monaco[95,20,16,15], A. Mora[96], M. Moresco[4,5], C. Moretti[20,15,16,14], L. Moscardini[4,5,21], R. Nakajima[89], C. Neissner[97,34], R. C. Nichol[98], S.-M. Niemi[9], C. Padilla[97], S. Paltani[54], F. Pasian[20], K. Pedersen[99], W. J. Percival[100,101,102], V. Pettorino[9], A. Pezzotta[19], S. Pires[79], G. Polenta[59], M. Poncet[103], L. A. Popa[104], C. Porciani[89], L. Pozzetti[5], F. Raison[64], A. Renzi[3,56], J. Rhodes[69], G. Riccio[25], I. Risso[19,23], E. Romelli[20], M. Roncarelli[5], R. Saglia[65,64], Z. Sakr[105,106,107], D. Sapone[108], B. Sartoris[65,20], J. A. Schewtschenko[41], M. Schirmer[75], P. Schneider[89], T. Schrabback[109], A. Secroun[57], G. Seidel[75], S. Serrano[110,111,112], P. Simon[89], C. Sirignano[3,56], G. Sirri[21], L. Stanco[56], J.-L. Starck[79], J. Steinwagner[64], P. Tallada-Crespí[33,34], A. N. Taylor[41], H. I. Teplitz[113], I. Tereno[52,114], N. Tessore[77,51], S. Toft[115,116], R. Toledo-Moreo[117], F. Torradeflot[34,33], I. Tutusaus[112,110,106], L. Valenziano[5,60], J. Valiviita[81,82], T. Vassallo[20], A. Veropalumbo[19,23,22], Y. Wang[113], J. Weller[65,64], A. Zacchei[20,15], E. Zucca[5], V. Allevato[25], M. Ballardini[118,119,5], E. Bozzo[54], C. Burigana[1,60], R. Cabanac[106], M. Calabrese[120,32], A. Cappi[121,5], J. A. Escartin Vigo[64], R. Maoli[122,18], J. Martín-Fleitas[123], S. Matthew[41], M. Maturi[105,124], R. B. Metcalf[4,5], M. Pöntinen[81], V. Scottez[13,125], M. Sereno[5,21], M. Tenti[21], M. Viel[15,20,14,16,126], M. Wiesmann[67], Y. Akrami[127,128], I. T. Andika[129,130], S. Anselmi[56,3,131], M. Archidiacono[86,87], F. Atrio-Barandela[132], D. Bertacca[3,2,56], M. Bethermin[133], A. Blanchard[106], L. Blot[134,83], M. Bonici[100,32], S. Borgani[95,15,20,16,126], M. L. Brown[42], S. Bruton[135], A. Calabro[18], B. Camacho Quevedo[15,14,20], F. Caro[18], C. S. Carvalho[114], T. Castro[20,16,15,126], F. Cogato[4,5], S. Conseil[45], A. R. Cooray[136], O. Cucciati[5], S. Davini[23], G. Desprez[8], A. Díaz-Sánchez[137], J. J. Diaz[40], S. Di Domizio[22,23], J. M. Diego[138], M. Y. Elkhashab[20,16,95,15], A. Enia[5], Y. Fang[65], A. Finoguenov[81], A. Franco[139,140,141], K. Ganga[92], J. García-Bellido[127], T. Gasparetto[18], V. Gautard[6], E. Gaztanaga[112,110,142], F. Giacomini[21], F. Gianotti[5], G. Gozaliasl[143,81], M. Guidi[10,5], C. M. Gutierrez[72], A. Hall[41], C. Hernández-Monteagudo[144,40], H. Hildebrandt[145], J. Hjorth[99], J. J. E. Kajava[146,147], Y. Kang[54], V. Kansal[148,149], D. Karagiannis[118,150], K. Kiiveri[78], J. Kim[62], C. C. Kirkpatrick[78], S. Kruk[44], L. Legrand[151,152], M. Lembo[12,118,119], F. Lepori[153], G. F. Lesci[4,5], J. Lesgourgues[35], L. Leuzzi[5], T. I. Liaudat[154], A. Loureiro[155,156], J. Macias-Perez[157], F. Mannucci[158], C. J. A. P. Martins[159,26], L. Maurin[55], M. Miluzio[44,160], G. Morgante[5], K. Naidoo[142,77], P. Natoli[118,119], A. Navarro-Alsina[89], S. Nesseris[127], D. Paoletti[5,60], F. Passalacqua[3,56], K. Paterson[75], L. Patrizii[21], A. Pisani[57], D. Potter[153], S. Quai[4,5], M. Radovich[2], S. Sacquegna[161], M. Sahlén[162], D. B. Sanders[38], E. Sarpa[14,126,16], A. Schneider[153], D. Sciotti[18,90], E. Sellentin[163,17], F. Shankar[164], A. Shulevski[165,8,17,166], L. C. Smith[167], J. G. Sorce[168,55], K. Tanidis[62], C. Tao[57], G. Testera[23], R. Teyssier[169], S. Tosi[22,23,19], A. Troja[3,56], M. Tucci[54], A. Venhola[170], D. Vergani[5], G. Verza[171,⋆⋆], P. Vielzeuf[57], and N. A. Walton[167]

[1] INAF, Istituto di Radioastronomia, Via Piero Gobetti 101, 40129 Bologna, Italy
[2] INAF – Osservatorio Astronomico di Padova, Via dell'Osservatorio 5, 35122 Padova, Italy

[3] Dipartimento di Fisica e Astronomia "G. Galilei", Università di Padova, Via Marzolo 8, 35131 Padova, Italy
[4] Dipartimento di Fisica e Astronomia "Augusto Righi" – Alma Mater Studiorum Università di Bologna, via Piero Gobetti 93/2, 40129 Bologna, Italy
[5] INAF – Osservatorio di Astrofisica e Scienza dello Spazio di Bologna, Via Piero Gobetti 93/3, 40129 Bologna, Italy
[6] CEA Saclay, DFR/IRFU, Service d'Astrophysique, Bat. 709, 91191 Gif-sur-Yvette, France
[7] SRON Netherlands Institute for Space Research, Landleven 12, 9747 AD Groningen, The Netherlands
[8] Kapteyn Astronomical Institute, University of Groningen, PO Box 800, 9700 AV Groningen, The Netherlands
[9] European Space Agency/ESTEC, Keplerlaan 1, 2201 AZ Noordwijk, The Netherlands
[10] Dipartimento di Fisica e Astronomia, Università di Bologna, Via Gobetti 93/2, 40129 Bologna, Italy
[11] Department of Physics and Astronomy, University of British Columbia, Vancouver, BC V6T 1Z1, Canada
[12] Institut d'Astrophysique de Paris, UMR 7095, CNRS, and Sorbonne Université, 98 bis boulevard Arago, 75014 Paris, France
[13] Institut d'Astrophysique de Paris, 98bis Boulevard Arago, 75014 Paris, France
[14] SISSA, International School for Advanced Studies, Via Bonomea 265, 34136 Trieste TS, Italy
[15] IFPU, Institute for Fundamental Physics of the Universe, via Beirut 2, 34151 Trieste, Italy
[16] INFN, Sezione di Trieste, Via Valerio 2, 34127 Trieste TS, Italy
[17] Leiden Observatory, Leiden University, Einsteinweg 55, 2333 CC Leiden, The Netherlands
[18] INAF – Osservatorio Astronomico di Roma, Via Frascati 33, 00078 Monteporzio Catone, Italy
[19] INAF – Osservatorio Astronomico di Brera, Via Brera 28, 20122 Milano, Italy
[20] INAF – Osservatorio Astronomico di Trieste, Via G. B. Tiepolo 11, 34143 Trieste, Italy
[21] INFN – Sezione di Bologna, Viale Berti Pichat 6/2, 40127 Bologna, Italy
[22] Dipartimento di Fisica, Università di Genova, Via Dodecaneso 33, 16146 Genova, Italy
[23] INFN-Sezione di Genova, Via Dodecaneso 33, 16146 Genova, Italy
[24] Department of Physics "E. Pancini", University Federico II, Via Cinthia 6, 80126 Napoli, Italy
[25] INAF-Osservatorio Astronomico di Capodimonte, Via Moiariello 16, 80131 Napoli, Italy
[26] Instituto de Astrofísica e Ciências do Espaço, Universidade do Porto, CAUP, Rua das Estrelas, 4150-762 Porto, Portugal
[27] Faculdade de Ciências da Universidade do Porto, Rua do Campo de Alegre, 4150-007 Porto, Portugal
[28] European Southern Observatory, Karl-Schwarzschild-Str. 2, 85748 Garching, Germany
[29] Dipartimento di Fisica, Università degli Studi di Torino, Via P. Giuria 1, 10125 Torino, Italy
[30] INFN – Sezione di Torino, Via P. Giuria 1, 10125 Torino, Italy
[31] INAF – Osservatorio Astrofisico di Torino, Via Osservatorio 20, 10025 Pino Torinese (TO), Italy
[32] INAF – IASF Milano, Via Alfonso Corti 12, 20133 Milano, Italy
[33] Centro de Investigaciones Energéticas, Medioambientales y Tecnológicas (CIEMAT), Avenida Complutense 40, 28040 Madrid, Spain
[34] Port d'Informació Científica, Campus UAB, C. Albareda s/n, 08193 Bellaterra (Barcelona), Spain
[35] Institute for Theoretical Particle Physics and Cosmology (TTK), RWTH Aachen University, 52056 Aachen, Germany
[36] Deutsches Zentrum für Luft- und Raumfahrt e. V. (DLR), Linder Höhe, 51147 Köln, Germany
[37] INFN Section of Naples, Via Cinthia 6, 80126 Napoli, Italy
[38] Institute for Astronomy, University of Hawaii, 2680 Woodlawn Drive, Honolulu, HI 96822, USA
[39] Dipartimento di Fisica e Astronomia "Augusto Righi" – Alma Mater Studiorum Università di Bologna, Viale Berti Pichat 6/2, 40127 Bologna, Italy
[40] Instituto de Astrofísica de Canarias, 38205 La Laguna, Tenerife, Spain
[41] Institute for Astronomy, University of Edinburgh, Royal Observatory, Blackford Hill, Edinburgh EH9 3HJ, UK
[42] Jodrell Bank Centre for Astrophysics, Department of Physics and Astronomy, University of Manchester, Oxford Road, Manchester M13 9PL, UK
[43] European Space Agency/ESRIN, Largo Galileo Galilei 1, 00044 Frascati, Roma, Italy
[44] ESAC/ESA, Camino Bajo del Castillo, s/n., Urb. Villafranca del Castillo, 28692 Villanueva de la Cañada, Madrid, Spain
[45] Université Claude Bernard Lyon 1, CNRS/IN2P3, IP2I Lyon, UMR 5822, Villeurbanne 69100, France
[46] Aix-Marseille Université, CNRS, CNES, LAM, Marseille, France
[47] Institut de Ciències del Cosmos (ICCUB), Universitat de Barcelona (IEEC-UB), Martí i Franquès 1, 08028 Barcelona, Spain
[48] Institució Catalana de Recerca i Estudis Avançats (ICREA), Passeig de Lluís Companys 23, 08010 Barcelona, Spain
[49] Institut de Ciencies de l'Espai (IEEC-CSIC), Campus UAB, Carrer de Can Magrans, s/n Cerdanyola del Vallés, 08193 Barcelona, Spain
[50] UCB Lyon 1, CNRS/IN2P3, IUF, IP2I Lyon, 4 rue Enrico Fermi, 69622 Villeurbanne, France
[51] Mullard Space Science Laboratory, University College London, Holmbury St Mary, Dorking, Surrey RH5 6NT, UK
[52] Departamento de Física, Faculdade de Ciências, Universidade de Lisboa, Edifício C8, Campo Grande, 1749-016 Lisboa, Portugal
[53] Instituto de Astrofísica e Ciências do Espaço, Faculdade de Ciências, Universidade de Lisboa, Campo Grande, 1749-016 Lisboa, Portugal
[54] Department of Astronomy, University of Geneva, ch. d'Ecogia 16, 1290 Versoix, Switzerland
[55] Université Paris-Saclay, CNRS, Institut d'astrophysique spatiale, 91405, Orsay, France
[56] INFN – Padova, Via Marzolo 8, 35131 Padova, Italy
[57] Aix-Marseille Université, CNRS/IN2P3, CPPM, Marseille, France
[58] INAF-Istituto di Astrofisica e Planetologia Spaziali, via del Fosso del Cavaliere, 100, 00100 Roma, Italy
[59] Space Science Data Center, Italian Space Agency, via del Politecnico snc, 00133 Roma, Italy
[60] INFN-Bologna, Via Irnerio 46, 40126 Bologna, Italy
[61] School of Physics, HH Wills Physics Laboratory, University of Bristol, Tyndall Avenue, Bristol BS8 1TL, UK
[62] Department of Physics, Oxford University, Keble Road, Oxford OX1 3RH, UK
[63] University Observatory, LMU Faculty of Physics, Scheinerstr. 1, 81679 Munich, Germany
[64] Max Planck Institute for Extraterrestrial Physics, Giessenbachstr. 1, 85748 Garching, Germany
[65] Universitäts-Sternwarte München, Fakultät für Physik, Ludwig-Maximilians-Universität München, Scheinerstr. 1, 81679 München, Germany
[66] National Research Council, Herzberg Astronomy and Astrophysics Research Centre, 5071 W. Saanich Rd. Victoria, BC V9E 2E7, Canada
[67] Institute of Theoretical Astrophysics, University of Oslo, PO Box 1029 Blindern, 0315 Oslo, Norway
[68] Caltech/IPAC, 1200 E. California Blvd., Pasadena, CA 91125, USA

[69] Jet Propulsion Laboratory, California Institute of Technology, 4800 Oak Grove Drive, Pasadena, CA 91109, USA
[70] Technical University of Denmark, Elektrovej 327, 2800 Kgs. Lyngby, Denmark
[71] Cosmic Dawn Center (DAWN), Denmark
[72] Instituto de Astrofísica de Canarias, 38205 La Laguna; Universidad de La Laguna, Dpto. Astrofísica, 38206 La Laguna, Tenerife, Spain
[73] Université PSL, Observatoire de Paris, Sorbonne Université, CNRS, LERMA, 75014 Paris, France
[74] Université Paris-Cité, 5 Rue Thomas Mann, 75013 Paris, France
[75] Max-Planck-Institut für Astronomie, Königstuhl 17, 69117 Heidelberg, Germany
[76] NASA Goddard Space Flight Center, Greenbelt, MD 20771, USA
[77] Department of Physics and Astronomy, University College London, Gower Street, London WC1E 6BT, UK
[78] Department of Physics and Helsinki Institute of Physics, Gustaf Hällströmin katu 2, University of Helsinki, 00014 Helsinki, Finland
[79] Université Paris-Saclay, Université Paris Cité, CEA, CNRS, AIM, 91191 Gif-sur-Yvette, France
[80] Université de Genève, Département de Physique Théorique and Centre for Astroparticle Physics, 24 quai Ernest-Ansermet, 1211 Genève 4, Switzerland
[81] Department of Physics, PO Box 64, University of Helsinki, 00014 Helsinki, Finland
[82] Helsinki Institute of Physics, Gustaf Hällströmin katu 2, University of Helsinki, 00014 Helsinki, Finland
[83] Laboratoire d'etude de l'Univers et des phenomenes eXtremes, Observatoire de Paris, Université PSL, Sorbonne Université, CNRS, 92190 Meudon, France
[84] SKAO, Jodrell Bank, Lower Withington, Macclesfield SK11 9FT, UK
[85] Centre de Calcul de l'IN2P3/CNRS, 21 avenue Pierre de Coubertin 69627 Villeurbanne Cedex, France
[86] Dipartimento di Fisica "Aldo Pontremoli", Università degli Studi di Milano, Via Celoria 16, 20133 Milano, Italy
[87] INFN-Sezione di Milano, Via Celoria 16, 20133 Milano, Italy
[88] University of Applied Sciences and Arts of Northwestern Switzerland, School of Computer Science, 5210 Windisch, Switzerland
[89] Universität Bonn, Argelander-Institut für Astronomie, Auf dem Hügel 71, 53121 Bonn, Germany
[90] INFN-Sezione di Roma, Piazzale Aldo Moro 2, c/o Dipartimento di Fisica, Edificio G. Marconi, 00185 Roma, Italy
[91] Department of Physics, Institute for Computational Cosmology, Durham University, South Road, Durham DH1 3LE, UK
[92] Université Paris Cité, CNRS, Astroparticule et Cosmologie, 75013 Paris, France
[93] CNRS-UCB International Research Laboratory, Centre Pierre Binétruy, IRL2007, CPB-IN2P3, Berkeley, USA
[94] Institute of Physics, Laboratory of Astrophysics, Ecole Polytechnique Fédérale de Lausanne (EPFL), Observatoire de Sauverny, 1290 Versoix, Switzerland
[95] Dipartimento di Fisica – Sezione di Astronomia, Università di Trieste, Via Tiepolo 11, 34131 Trieste, Italy
[96] Telespazio UK S.L. for European Space Agency (ESA), Camino bajo del Castillo, s/n, Urbanizacion Villafranca del Castillo, Villanueva de la Cañada, 28692 Madrid, Spain
[97] Institut de Física d'Altes Energies (IFAE), The Barcelona Institute of Science and Technology, Campus UAB, 08193 Bellaterra (Barcelona), Spain
[98] School of Mathematics and Physics, University of Surrey, Guildford, Surrey GU2 7XH, UK
[99] DARK, Niels Bohr Institute, University of Copenhagen, Jagtvej 155, 2200 Copenhagen, Denmark
[100] Waterloo Centre for Astrophysics, University of Waterloo, Waterloo, Ontario N2L 3G1, Canada
[101] Department of Physics and Astronomy, University of Waterloo, Waterloo, Ontario N2L 3G1, Canada
[102] Perimeter Institute for Theoretical Physics, Waterloo, Ontario N2L 2Y5, Canada
[103] Centre National d'Etudes Spatiales – Centre spatial de Toulouse, 18 avenue Edouard Belin, 31401 Toulouse Cedex 9, France
[104] Institute of Space Science, Str. Atomistilor, no. 409 Măgurele, Ilfov, 077125, Romania
[105] Institut für Theoretische Physik, University of Heidelberg, Philosophenweg 16, 69120 Heidelberg, Germany
[106] Institut de Recherche en Astrophysique et Planétologie (IRAP), Université de Toulouse, CNRS, UPS, CNES, 14 Av. Edouard Belin, 31400 Toulouse, France
[107] Université St Joseph; Faculty of Sciences, Beirut, Lebanon
[108] Departamento de Física, FCFM, Universidad de Chile, Blanco Encalada 2008, Santiago, Chile
[109] Universität Innsbruck, Institut für Astro- und Teilchenphysik, Technikerstr. 25/8, 6020 Innsbruck, Austria
[110] Institut d'Estudis Espacials de Catalunya (IEEC), Edifici RDIT, Campus UPC, 08860 Castelldefels, Barcelona, Spain
[111] Satlantis, University Science Park, Sede Bld 48940, Leioa-Bilbao, Spain
[112] Institute of Space Sciences (ICE, CSIC), Campus UAB, Carrer de Can Magrans, s/n, 08193 Barcelona, Spain
[113] Infrared Processing and Analysis Center, California Institute of Technology, Pasadena, CA 91125, USA
[114] Instituto de Astrofísica e Ciências do Espaço, Faculdade de Ciências, Universidade de Lisboa, Tapada da Ajuda, 1349-018 Lisboa, Portugal
[115] Cosmic Dawn Center (DAWN)
[116] Niels Bohr Institute, University of Copenhagen, Jagtvej 128, 2200 Copenhagen, Denmark
[117] Universidad Politécnica de Cartagena, Departamento de Electrónica y Tecnología de Computadoras, Plaza del Hospital 1, 30202 Cartagena, Spain
[118] Dipartimento di Fisica e Scienze della Terra, Università degli Studi di Ferrara, Via Giuseppe Saragat 1, 44122 Ferrara, Italy
[119] Istituto Nazionale di Fisica Nucleare, Sezione di Ferrara, Via Giuseppe Saragat 1, 44122 Ferrara, Italy
[120] Astronomical Observatory of the Autonomous Region of the Aosta Valley (OAVdA), Loc. Lignan 39, 11020 Nus (Aosta Valley), Italy
[121] Université Côte d'Azur, Observatoire de la Côte d'Azur, CNRS, Laboratoire Lagrange, Bd de l'Observatoire, CS 34229, 06304 Nice cedex 4, France
[122] Dipartimento di Fisica, Sapienza Università di Roma, Piazzale Aldo Moro 2, 00185 Roma, Italy
[123] Aurora Technology for European Space Agency (ESA), Camino bajo del Castillo, s/n, Urbanizacion Villafranca del Castillo, Villanueva de la Cañada, 28692 Madrid, Spain
[124] Zentrum für Astronomie, Universität Heidelberg, Philosophenweg 12, 69120 Heidelberg, Germany
[125] ICL, Junia, Université Catholique de Lille, LITL, 59000 Lille, France
[126] ICSC – Centro Nazionale di Ricerca in High Performance Computing, Big Data e Quantum Computing, Via Magnanelli 2, Bologna, Italy
[127] Instituto de Física Teórica UAM-CSIC, Campus de Cantoblanco, 28049 Madrid, Spain

[128] CERCA/ISO, Department of Physics, Case Western Reserve University, 10900 Euclid Avenue, Cleveland, OH 44106, USA
[129] Technical University of Munich, TUM School of Natural Sciences, Physics Department, James-Franck-Str. 1, 85748 Garching, Germany
[130] Max-Planck-Institut für Astrophysik, Karl-Schwarzschild-Str. 1, 85748 Garching, Germany
[131] Laboratoire Univers et Théorie, Observatoire de Paris, Université PSL, Université Paris Cité, CNRS, 92190 Meudon, France
[132] Departamento de Física Fundamental. Universidad de Salamanca. Plaza de la Merced s/n, 37008 Salamanca, Spain
[133] Université de Strasbourg, CNRS, Observatoire astronomique de Strasbourg, UMR 7550, 67000 Strasbourg, France
[134] Center for Data-Driven Discovery, Kavli IPMU (WPI), UTIAS, The University of Tokyo, Kashiwa, Chiba 277-8583, Japan
[135] California Institute of Technology, 1200 E California Blvd, Pasadena, CA 91125, USA
[136] Department of Physics & Astronomy, University of California Irvine, Irvine CA 92697, USA
[137] Departamento Física Aplicada, Universidad Politécnica de Cartagena, Campus Muralla del Mar, 30202 Cartagena, Murcia, Spain
[138] Instituto de Física de Cantabria, Edificio Juan Jordá, Avenida de los Castros, 39005 Santander, Spain
[139] INFN, Sezione di Lecce, Via per Arnesano, CP-193, 73100 Lecce, Italy
[140] Department of Mathematics and Physics E. De Giorgi, University of Salento, Via per Arnesano, CP-I93, 73100 Lecce, Italy
[141] INAF-Sezione di Lecce, c/o Dipartimento Matematica e Fisica, Via per Arnesano, 73100 Lecce, Italy
[142] Institute of Cosmology and Gravitation, University of Portsmouth, Portsmouth PO1 3FX, UK
[143] Department of Computer Science, Aalto University, PO Box 15400, Espoo 00 076, Finland
[144] Universidad de La Laguna, Dpto. Astrofísica, 38206 La Laguna, Tenerife, Spain
[145] Ruhr University Bochum, Faculty of Physics and Astronomy, Astronomical Institute (AIRUB), German Centre for Cosmological Lensing (GCCL), 44780 Bochum, Germany
[146] Department of Physics and Astronomy, Vesilinnantie 5, University of Turku, 20014 Turku, Finland
[147] Serco for European Space Agency (ESA), Camino bajo del Castillo, s/n, Urbanizacion Villafranca del Castillo, Villanueva de la Cañada, 28692 Madrid, Spain
[148] ARC Centre of Excellence for Dark Matter Particle Physics, Melbourne, Australia
[149] Centre for Astrophysics & Supercomputing, Swinburne University of Technology, Hawthorn, Victoria 3122, Australia
[150] Department of Physics and Astronomy, University of the Western Cape, Bellville, Cape Town 7535, South Africa
[151] DAMTP, Centre for Mathematical Sciences, Wilberforce Road, Cambridge CB3 0WA, UK
[152] Kavli Institute for Cosmology Cambridge, Madingley Road, Cambridge CB3 0HA, UK
[153] Department of Astrophysics, University of Zurich, Winterthurerstrasse 190, 8057 Zurich, Switzerland
[154] IRFU, CEA, Université Paris-Saclay 91191 Gif-sur-Yvette Cedex, France
[155] Oskar Klein Centre for Cosmoparticle Physics, Department of Physics, Stockholm University, Stockholm 106 91, Sweden
[156] Astrophysics Group, Blackett Laboratory, Imperial College London, London SW7 2AZ, UK
[157] Univ. Grenoble Alpes, CNRS, Grenoble INP, LPSC-IN2P3, 53, Avenue des Martyrs, 38000 Grenoble, France
[158] INAF-Osservatorio Astrofisico di Arcetri, Largo E. Fermi 5, 50125 Firenze, Italy
[159] Centro de Astrofísica da Universidade do Porto, Rua das Estrelas, 4150-762 Porto, Portugal
[160] HE Space for European Space Agency (ESA), Camino bajo del Castillo, s/n, Urbanizacion Villafranca del Castillo, Villanueva de la Cañada, 28692 Madrid, Spain
[161] INAF – Osservatorio Astronomico d'Abruzzo, Via Maggini, 64100 Teramo, Italy
[162] Theoretical astrophysics, Department of Physics and Astronomy, Uppsala University, Box 516, 751 37 Uppsala, Sweden
[163] Mathematical Institute, University of Leiden, Einsteinweg 55, 2333 CA Leiden, The Netherlands
[164] School of Physics & Astronomy, University of Southampton, Highfield Campus, Southampton SO17 1BJ, UK
[165] ASTRON, the Netherlands Institute for Radio Astronomy, Postbus 2, 7990 AA, Dwingeloo, The Netherlands
[166] Center for Advanced Interdisciplinary Research, Ss. Cyril and Methodius University in Skopje, Macedonia
[167] Institute of Astronomy, University of Cambridge, Madingley Road, Cambridge CB3 0HA, UK
[168] Univ. Lille, CNRS, Centrale Lille, UMR 9189 CRIStAL, 59000 Lille, France
[169] Department of Astrophysical Sciences, Peyton Hall, Princeton University, Princeton, NJ 08544, USA
[170] Space physics and astronomy research unit, University of Oulu, Pentti Kaiteran katu 1, 90014 Oulu, Finland
[171] Center for Computational Astrophysics, Flatiron Institute, 162 5th Avenue, New York, NY 10010, USA

⋆ Corresponding author: m.giulietti@ira.inaf.it
⋆⋆ Deceased.

Appendix A: SED of individual sources

In the following, we report the best-fit SED for the 19 objects among the 53 LOFAR ILT-covered objects that have at least one FIR counterpart.

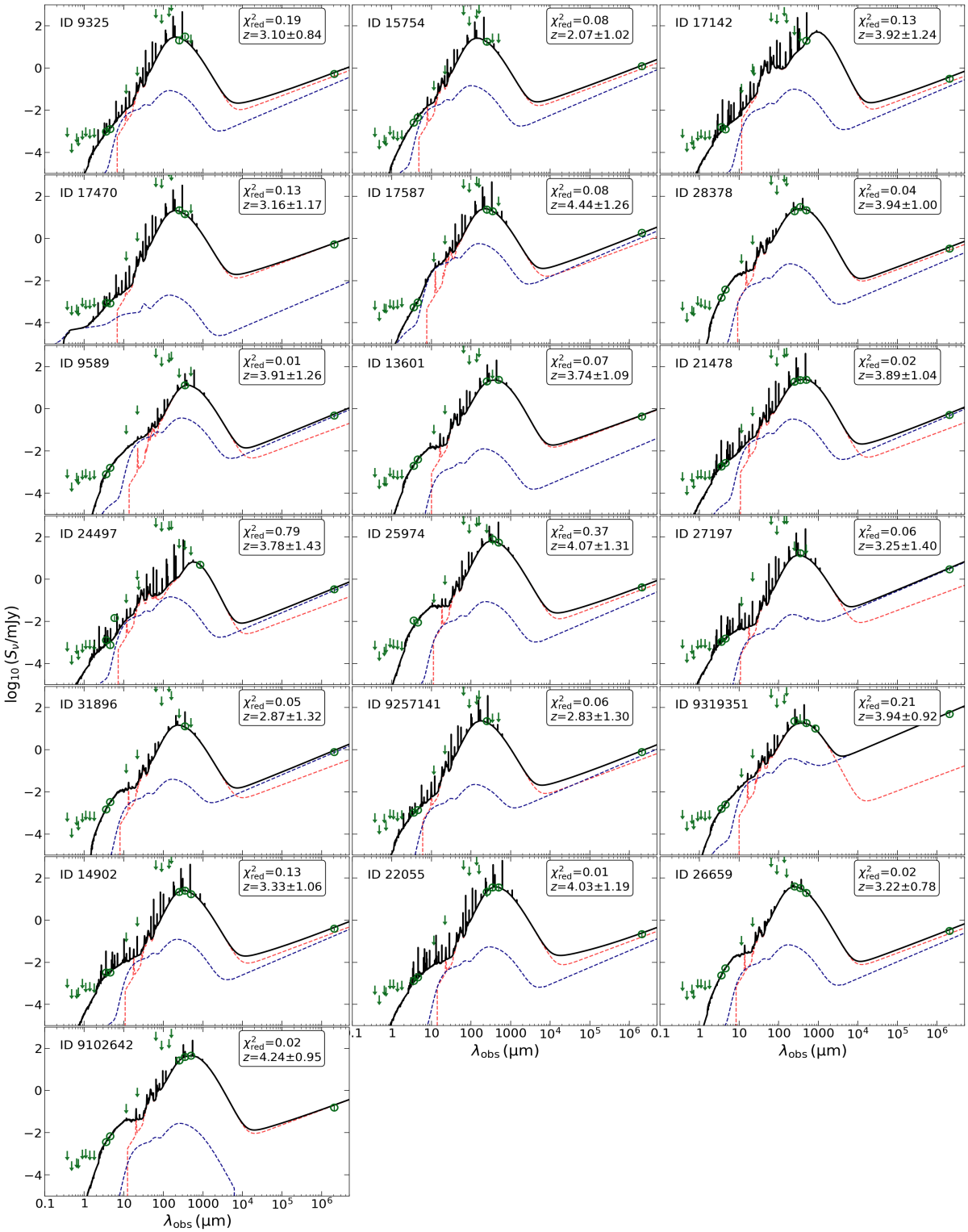


Fig. A.1. Best-fit SED (solid grey lines) for the 19 sources for which at least one photometric detection in the FIR is available. Symbols and lines have the same meaning as in Fig. 10. Reported wavelengths are in the observed frame.

Appendix B: Isolated E-dark sources with no LOFAR ILT coverage

Among our sample of 88 isolated E-dark galaxies, 35 of them are not covered by the LOFAR ILT high-resolution image, and therefore no estimate of r nor T_b is available. Eight sources have at least one photometric point in SPIRE and/or SCUBA-2. We repeated the SED fitting described in Sect. 4.3 also for this sample. Given that we have no prior knowledge on the AGN contribution to the radio emission, we allowed the radio-loudness parameter to vary as $R_{AGN} = 0.0, 0.1, 1, 10, 100, 1000$. The best-fit SEDs for the sources with FIR counterparts are shown in Fig. B.1, while the IRRC is shown in Fig. B.2.

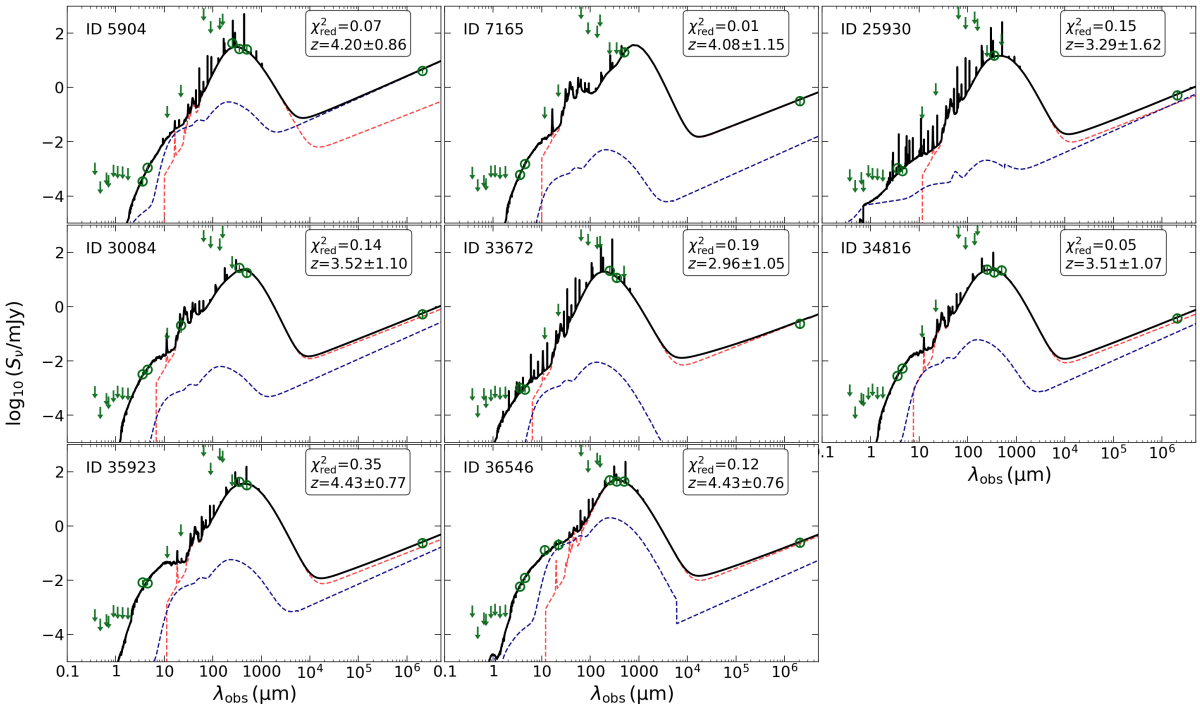


Fig. B.1. Same as Fig. A.1 for the sample of 8/35 sources with at least one FIR counterpart and without LOFAR ILT coverage.

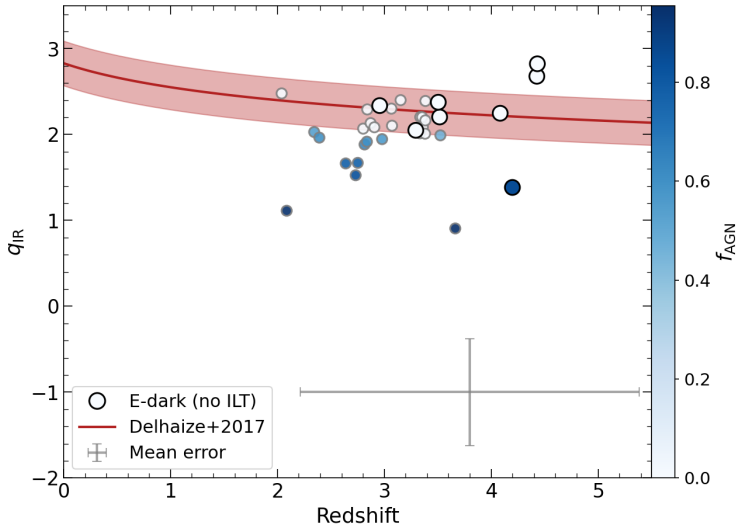


Fig. B.2. Same as the left panel of Fig. 5 for the 35 objects without LOFAR ILT coverage. Objects with at least one SPIRE detection are marked with larger symbols, while sources without SPIRE detections are shown with smaller symbols.